Journal of Fluids and Structures 117 (2023) 103828

Contents lists available at ScienceDirect

Journal of Fluids and Structures

journal homepage: www.elsevier.com/locate/jfs

Aeroelastic response of an elastically mounted 2-DOF airfoil and its gust-induced oscillations

K. Boulbrachene, M. Breuer *

Professur für Strömungsmechanik, Helmut-Schmidt-Universität Hamburg, D-22043 Hamburg, Germany

ARTICLE INFO

Article history:
Received 18 July 2022
Received in revised form 16 December 2022
Accepted 22 December 2022
Available online xxxx

Keywords:
Wind gust
Split velocity method
Fluid–structure interaction (FSI)
2-DOF aeroelastic oscillations
Limit-cycle oscillation (LCO)
Airfoil flutter
Large-eddy simulation (LES)
Energy analysis

ABSTRACT

The paper is concerned with numerical investigations on the effect of vertical wind gusts on airfoils in a parameter range relevant for Micro-Air Vehicles. Using a simplified substitute model instead of an elastic wing, a rigid but elastically mounted airfoil with two degrees of freedom (heave and pitch) is considered. The coupled problem is tackled by a partitioned fluid–structure interaction coupling scheme based on the large-eddy simulation (LES) technique and a rigid-body solver. In order to describe the effect of deterministic 1-cosine gusts of different gust lengths and gust strengths, the split velocity method (SVM) is incorporated into the simulation framework relying on the Arbitrary Lagrangian–Eulerian (ALE) formulation on temporally varying control volumes. First the flow fields and the corresponding aerodynamic forces during the direct airfoil–gust interaction are compared for a fixed and an elastically mounted airfoil. The intrinsic study on the elastic case includes nine different gust scenarios in the transitional Reynolds number regime in order to investigate the resulting flow fields and motion patterns and to answer the question whether limit-cycle oscillations (LCO) or even flutter can be induced. The results show that in seven of the studied cases, the airfoil–gust interaction leads to sustained heave and pitch oscillations of bounded amplitudes (i.e., LCO). Further investigations clarify that this can be physically attributed to the laminar separation taking place on the upper and lower surfaces of the airfoil. The two strongest gust cases, however, excite the airfoil to levels above its critical angle of attack and triggered a pitch-induced diverging flutter. An energy analysis of both characteristic scenarios (i.e., LCO and flutter) further elucidates the differences between both cases. The former case is driven by the heave motion, whereas the pitch DOF acts as an energy sink. Contrarily, in the case of flutter the pitching motion is powering the coupled system, whereas the heave motion dissipates energy.

1. Introduction

The unsteady aerodynamics of airfoils and their associated aeroelastic response have been an active field of research during the last century. The preceding transient aerodynamic models were potential flow-based models (Theodorsen, 1935; von Kármán and Sears, 1938) and were followed by studies addressing flow separation, formation and shedding of leading-edge vortices, and dynamic stall (McCroskey, 1982; Ekaterinaris and Platzer, 1998). While small deflections are typical for aerospace applications, energy harvesting applications, for instance, include large-amplitude oscillations. Depending on the application intended, the techniques employed to analyze and investigate these systems differ. For

* Corresponding author.
E-mail address: breuer@hsu-hh.de (M. Breuer).

https://doi.org/10.1016/j.jfluidstructs.2022.103828

example, linearized force models are found suitable for very small deflections, however, large-amplitude oscillations such as dynamic stall act as a source of nonlinearity. Moreover, the accompanying formation and shedding of leading-edge vortices results in highly transient loads which in turn pose considerable challenges to develop models capturing all the physics involved (Eldredge and Jones, 2019). Therefore, the accurate forecast of the aeroelastic response including all the possible extreme scenarios by means of experimental and numerical simulations is essential to ensure a reliable design process. A brief literature review focusing on the oscillatory behavior of airfoils subjected to different flow conditions is given in the following.

The wind tunnel experiments of a freely pitching NACA 0012 airfoil in the transitional Re regime conducted by Poirel et al. (2008) have extended the field in which the aerodynamic nonlinearities influence the aeroelastic stability. Unlike the stall flutter (known to be resulting from the periodic flow separation and reattachment at high angles-of-attack) or the transonic flutter (essentially resulting from shock waves moving along the wing's surface) (see Dowell and Tang (2002), Dowell et al. (2003)), Poirel et al. (2008) attributed the self-sustained oscillations found to the nonlinear aerodynamic load associated with the laminar boundary layer separation at the airfoil's trailing edge.

In order to obtain further insights into the physics involved in the course of the self-sustained oscillations, Poirel and Yuan (2010) performed large-eddy simulations (LES) of the flow around the airfoil undergoing a prescribed pitch motion taken from the pitch motion measured experimentally. It was found that the sustained oscillation is linked to the negative aerodynamic damping resulting from the unsteadiness of the trailing-edge laminar boundary-layer separation.

The complementary work of Poirel et al. (2011) conducted numerical simulations using an unsteady RANS solver and the SST k–ω model with low-Re number correction to study the laminar separation flutter (LSF). The results confirmed the key role of the laminar boundary layer separation on the initiation and maintenance of LSF. Moreover, the authors deduced that while high free-stream turbulence intensities tend to inhibit the sustained oscillations, the high frequency von Kármán shedding has no influence on the mechanisms maintaining the self-induced oscillations. Yuan et al. (2013) extended the simulation setup to include the heave degree of freedom (DOF). In contrast to the 1-DOF pitch system, minor contradictions with the experiments were found in the 2-DOF system which were attributed to the neglected dry friction in heave. Albeit the pitch-driven motion found (i.e., heave had relatively small amplitudes), the energy fed by the flow into the system was significantly amplified (three times larger).

Barnes and Visbal (2018b) coupled an implicit LES flow solver with a structural dynamics solver to explore pitching limit-cycle oscillations (LCO) on a rigid elastically mounted NACA 0012 airfoil operating at transitional Reynolds numbers. While for the low Reynolds numbers investigated sustained oscillations were found to grow naturally from rest, Reynolds numbers at the high end of the flutter regime demonstrated a bifurcation in different possible solution states. These appeared as emerging limit-cycle oscillations following an external disturbance or an initial condition and a static airfoil condition when no external excitation is applied. The latter case is essentially caused by the enhanced flow transition at higher Reynolds numbers which shortens the separation bubbles and diminishes their negative aerodynamic damping. Practically, external disturbances can be provided by atmospheric turbulence, abrupt changes in flight conditions, or wind gusts. For that reason, Barnes and Visbal (2018a) used the same 1-DOF aeroelastic configuration to subject the airfoil to a counterclockwise Taylor vortex gust. This transient vortical-gust/wing interaction was shown to be capable of eliciting laminar separation flutter which would not occur otherwise for the chosen Reynolds number.

Huntley et al. (2017) implemented two gust injection methods, namely, the split velocity method (SVM) and the field velocity method (FVM), into a flow solver and coupled that to a modal structural solver to predict the aeroelastic response of a flexible wing to a series of vertical gusts of the classical 1-cosine type. The results obtained by both methods were compared and noticeable differences in the solution were found for short wavelength gusts. Heinrich and Reimer (2013) implemented FVM (referred to as disturbance velocity approach in their work) and compared it to the resolved gust approach, a method in which the gust introduced at the far-field boundary is transported via an overset mesh. Based on these methods the interaction of a 1-cosine vertical gust penetrating a NACA 0012 wing with a horizontal tail plane (HTP) was simulated. The results of both methods were found to be in good agreement for gust wavelengths larger than two chord lengths. For short gusts, FVM over-predicted the lift peaks during the gust-HTP interaction as it failed to capture the wing's effect on the gust shape. Therefore, FVM was employed to perform aeroelastic simulations of a generic fighter aircraft and an A340 configuration encountering long vertical gusts. It is worth mentioning that for the last two aforementioned references, no flutter stability analysis was carried out. The advantages of SVM compared to FVM and its capabilities to deliver physically reasonable results was also worked out in Boulbrachene et al. (2021). Menon and Mittal (2019) studied flow-induced airfoil pitch oscillations of a rigid airfoil using a sharp-interface immersed boundary method. Beside investigating the parameters affecting the dynamics of wing flutter, the authors demonstrated the use of energy maps (maps describing the energy exchange between the flow and the airfoil over a range of selected parameters) as a tool to analyze the complex flow-induced flutter response of a 1-DOF system. Using the same computational model, Menon and Mittal (2020) demonstrated a method based on energy maps to accurately predict the aeroelastic response of a pitching airfoil to transverse gusts. The method predicts the final stationary state of the system given an initial angle-of-attack induced by a perturbation (i.e., a gust).

In this paper, the aeroelastic response of a two degrees of freedom (heave and pitch) NACA 0012 airfoil in the transitional Reynolds number regime subjected to strong vertical wind gusts is numerically investigated based on LES. This parameter combination of moderate Reynolds number and high gust ratio is highly relevant for Micro-Air Vehicles. The effect of different gust parameters (wavelengths and amplitudes) on the dynamics of the airfoil is examined. Especially the question that should be answered is whether a certain gust can lead to limit-cycle oscillations or even flutter. Furthermore, the influence of different gust lengths and gust amplitudes on this phenomenon should be analyzed. The fluid–structure interaction setup without gusts has already been introduced by De Nayer et al. (2020) and validated against the experimental work of Wood et al. (2020). The simulation setup is slightly modified to accommodate the vertical gusts introduced. Wind gusts are applied by the split velocity method which was found in the previous studies to be capable of capturing the full interaction between the gust and the structure (Wales et al., 2014; Huntley et al., 2017; Badrya et al., 2019; Boulbrachene et al., 2021).

2. Wind gust modeling

In a recent study by Boulbrachene et al. (2021) a literature review on different approaches to inject wind gusts into the computational domain was given. Besides far-field boundary conditions and source-term formulations prescribed velocity methods are a common methodology especially in aeronautics. Advantages of the latter are that the gust can be injected directly in front of the structure of interest, which avoids strong damping effects by numerical dissipation and makes highly resolved grids in the entire computational domain superfluous. Thus, it is the method of choice for the planned studies on the flutter behavior of an airfoil subjected to vertical gusts.

2.1. Split velocity method (SVM)

The split velocity method was originally proposed by Wales et al. (2014). Its main idea lies on the decomposition of the total velocity u_i into two components, namely, a background velocity $\tilde{u}_i$ and a prescribed gust velocity $u_{g,i}$. The governing equations are then rearranged in order to solve for the background velocity $\tilde{u}_i$. SVM is known in the literature to be an extension of the former field velocity method (FVM). While FVM solely employs the Arbitrary Lagrangian–Eulerian (ALE) formulation of the governing equations (but without actual grid movement), SVM extends that by an additional source term accounting for the feedback effect. The detailed derivation of SVM for the Euler equations is provided in Wales et al. (2014) and for the Navier–Stokes equations in Huntley et al. (2016) and Boulbrachene et al. (2021). The governing equations solved for SVM on a fixed grid read:

$$\int_{V^{\mathrm{grid}}} \frac{\partial \rho}{\partial t}\, dV + \int_{S^{\mathrm{grid}}} \rho\,(\tilde{u}_j + u_{g,j}) \cdot n_j\, dS = 0\,, \tag{1}$$

$$\begin{aligned}\int_{V^{\mathrm{grid}}} \frac{\partial\left(\rho\,(\tilde{u}_i + u_{g,i})\right)}{\partial t}\, dV + \int_{S^{\mathrm{grid}}} \rho\,(\tilde{u}_i + u_{g,i})(\tilde{u}_j + u_{g,j}) \cdot n_j\, dS &= -\int_{S^{\mathrm{grid}}} \tau_{ij} \cdot n_j\, dS \\ &\quad - \int_{S^{\mathrm{grid}}} p \cdot n_i\, dS\,,\end{aligned} \tag{2}$$

where ρ is the density of the fluid, τ_{ij} is the stress tensor based on the total velocity u_i. n_j describes the unit normal vector of the control volume pointing outwards and V^{grid} denotes the volume of the undeformed grid. Upon the rearrangement of the equations (see Boulbrachene et al. (2021)) one obtains:

$$\frac{d}{dt}\int_{V^{\mathrm{grid}}\to V^*} \rho\, dV + \int_{S^{\mathrm{grid}}} \rho\,\tilde{u}_j \cdot n_j\, dS + \gamma \int_{S^{\mathrm{grid}}} \rho\, u_{g,j} \cdot n_j\, dS = 0\,, \tag{3}$$

$$\begin{aligned}\frac{d}{dt}\int_{V^{\mathrm{grid}}\to V^*} \rho\,\tilde{u}_i\, dV + \int_{S^{\mathrm{grid}}} \rho\,\tilde{u}_i\tilde{u}_j \cdot n_j\, dS + \gamma \int_{S^{\mathrm{grid}}} \rho\,\tilde{u}_i\, u_{g,j} \cdot n_j\, dS &= \int_{V^{\mathrm{grid}}} S_{\mathrm{momentum},i}\, dV \\ &\quad - \int_{S^{\mathrm{grid}}} \tau_{ij} \cdot n_j\, dS - \int_{S^{\mathrm{grid}}} p \cdot n_i\, dS,\end{aligned} \tag{4}$$

where the scaling factor γ is defined as $\gamma = \frac{V^*}{V^{\mathrm{grid}}}$, with V^* being the pseudo updated volume caused by the apparent grid movement associated with the prescribed velocity methods. The source term $S_{\mathrm{momentum},i}$ results from rearranging and simplifying Eq. (2) and reads:

$$S_{\mathrm{momentum},i} = -\rho\, \left\{ \frac{\partial u_{g,i}}{\partial t} + (\tilde{u}_j + u_{g,j}) \frac{\partial u_{g,i}}{\partial x_j} \right\}. \tag{5}$$

The system of Eqs. (3)–(5) is applicable to fluid flow predictions relying on fixed grids as used in Boulbrachene et al. (2021) for the flow around a fixed flat plate. In case of fluid–structure interaction (FSI) the ALE formulation (Breuer et al., 2012) is applied in the present investigation. Hence, the equations have to be re-formulated for a temporally varying domain, i.e., control volumes (CV) with time-dependent volumes $V(t)$ and surfaces $S(t)$. For this purpose, the grid velocity $u_{\mathrm{grid},j}$ with which the surface of a CV is moving has to be taken into account. The grid velocity is subtracted from the convective velocity (i.e., $\tilde{u}_j$) in the equations above. This yields the set of equations used to solve for the fluid flow:

$$\frac{d}{dt}\int_{V^n\to (V^{n+1})^*} \rho\, dV + \int_{S(t)} \rho\, \left(\tilde{u}_j - u_{\mathrm{grid},j}\right) \cdot n_j\, dS + \gamma \int_{S(t)} \rho\, u_{g,j} \cdot n_j\, dS = 0\,, \tag{6}$$

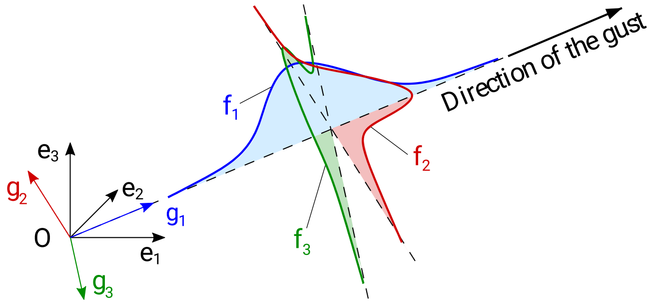

Fig. 1. Definition of the gust in the local basis $\mathcal{B}_1 = (O, \mathbf{g}_1, \mathbf{g}_2, \mathbf{g}_3)$.

$$\frac{d}{dt}\int_{V^n \to (V^{n+1})^*} \rho\, \tilde{u}_i\, dV + \int_{S(t)} \rho\, \tilde{u}_i \left(\tilde{u}_j - u_{\text{grid},j}\right) \cdot n_j\, dS + \gamma \int_{S(t)} \rho\, \tilde{u}_i\, u_{g,j} \cdot n_j\, dS = \int_{V(t)} S_{\text{momentum},i}\, dV - \int_{S(t)} \tau_{ij} \cdot n_j\, dS - \int_{S(t)} p \cdot n_i\, dS\,, \tag{7}$$

where V^n and V^{n+1} are the geometric cell volumes corresponding to the deformed grid at t^n and t^{n+1}, respectively. $(V^{n+1})^*$ is the updated deformed grid volume taking the additional pseudo volume change arising from the prescribed velocity method into account. It is worth mentioning that the geometric conservation law (GCL) (Demirdžić and Perić, 1988, 1990; Lesoinne and Farhat, 1996) is employed to suppress the contribution of the pseudo as well as the actual grid movement to the mass fluxes (by canceling out with the unsteady term in Eq. (6)). Hence, the mass conservation equation is reduced to:

$$\int_{S(t)} \rho\, \tilde{u}_j \cdot n_j\, dS = 0\,, \tag{8}$$

which is equivalent to the mass conservation equation for a fixed grid.

2.2. Gust velocity model

In the context of deterministic gust models the imposed analytical gust velocity $u_{g,i}$ is defined as (see Fig. 1):

$$u_{g,i}\big|_{\mathcal{B}_1}(t, \xi, \eta, \zeta) = A_g\, f_t(t)\;\; f_1(\xi)\;\; f_2(\eta)\;\; f_3(\zeta)\;\; g_1\,.$$

The constant A_g defines the strength of the gust and the function f_t the temporal evolution of the gust velocity. The functions f_1, f_2 and f_3 define the spatial distribution of the gust velocity in g_1, g_2 and g_3 direction, respectively.

For a vertical gust, the gust velocity consists of a single component pointing perpendicular to the streamwise direction. Therefore, the gust local basis is oriented such as $(\mathbf{g}_1, \mathbf{g}_2, \mathbf{g}_3) = (\mathbf{e}_3, \mathbf{e}_1, \mathbf{e}_2)$. In the present study, the prescribed gust is an Extreme Coherent gust (ECG) defined in the IEC-Standard (IEC-Standard, 2002) often denoted "1-cosine" shape. It varies in the streamwise direction and is convected downstream in time (i.e., $u_{g,i} = \left[0,\ 0,\ u_{g,3}(x_1, t)\right]$). Hence, f_t, f_1 and f_3 are equal to unity. The vertical gust component can be written in the Cartesian basis as:

$$u_{g,3}(x_1, t) = \begin{cases} \dfrac{A_g}{2}\left(1 + \cos\left(\dfrac{2\pi\left(x_1 - x_{g,1}(t)\right)}{L_g^{x_1}}\right)\right) & \text{for} \quad \left(x_1 - x_{g,1}\right) \in \left[-\dfrac{L_g^{x_1}}{2}, \dfrac{L_g^{x_1}}{2}\right] \\ 0 & \text{else}\,, \end{cases} \tag{9}$$

where A_g is the gust amplitude, $L_g^{x_1}$ is the gust length scale along the streamwise direction and $x_{g,1}(t)$ is the gust center coordinate. The introduction of this center coordinate (De Nayer et al., 2019) allows more control than the original shape. Based on the initial gust center coordinate $x_{g,1}^0$ and the gust convection velocity $u_{g,conv}$, the convected gust center is defined as:

$$x_{g,1}(t) = x_{g,1}^0 + (t - t_0)\, u_{g,conv}\,. \tag{10}$$

For a vertical gust, the source terms of the momentum equations are reduced to $S_{\text{momentum},i} = \left[0, 0, S_3(u_{g,3}(x_1, t))\right]$. Employing Eq. (5), the source term of the z-momentum equation reads:

$$S_3 = -\rho \left\{ \frac{\partial u_{g,3}}{\partial t} + \tilde{u}_1 \frac{\partial u_{g,3}}{\partial x_1} \right\}. \tag{11}$$

For the prescribed gust velocity (i.e., Eq. (9)), the temporal and spatial derivatives read:

$$\begin{aligned}
\frac{\partial u_{g,3}}{\partial t} &= +\frac{\pi\, A_g\, u_{g,conv}}{L_g^{x_1}} \sin\left(\frac{2\pi\,\left(x_1 - x_{g,1}(t)\right)}{L_g^{x_1}}\right)\,, \\
\frac{\partial u_{g,3}}{\partial x_1} &= -\frac{\pi\, A_g}{L_g^{x_1}} \sin\left(\frac{2\pi\,\left(x_1 - x_{g,1}(t)\right)}{L_g^{x_1}}\right)\,.
\end{aligned} \tag{12}$$

Substituting the derivatives (12) into Eq. (11) and simplifying the source term yields:

$$S_3(x_1, t) = -\rho\, \frac{\pi A_g}{L_g^{x_1}} \sin\left(\frac{2\pi\,\left(x_1 - x_{g,1}(t)\right)}{L_g^{x_1}}\right) \left\{u_{g,conv} - \tilde{u}_1\right\}. \tag{13}$$

The source term is a function of the coordinate x_1 and the time and it is coupled to the background velocity $\tilde{u}_1$. This coupling relies on the difference between the gust convection velocity and the streamwise velocity of the flow. It can be clearly seen from Eq. (13) that the source term vanishes if these two quantities are identical. This is anticipated as, for instance, one would expect no interaction between a uniform horizontal parallel flow and a vertical jet traveling with the same horizontal velocity downstream. However, the situation is different when these velocities do not match (i.e., when $u_{g,conv} > \tilde{u}_1$ or $u_{g,conv} < \tilde{u}_1$). For the former case, the jet would normally tend to accelerate the horizontal background velocity, and since the total momentum of the fluid is conserved, this is achieved by decelerating the vertical background velocity through the addition of a negative source term. In contrast (i.e., when $u_{g,conv} < \tilde{u}_1$), the jet would resist and block the horizontal background velocity and this is modeled by accelerating the vertical background velocity by means of an added positive source term. The effect of the gust amplitude on the resulting source terms lies on amplifying these terms for stronger gusts and mitigating their effects for weaker ones.

2.3. Convective boundary condition treatment

Employing SVM special care has to be taken to properly apply a convective boundary condition at outlets. For this type of boundary condition the convective transport equation is solved at an outlet patch:

$$\frac{\partial u_i}{\partial t} + \frac{\partial U_j^c u_i}{\partial x_j} = 0\,, \tag{14}$$

where U_j^c is the outlet convective velocity vector. Since in SVM the velocity is decomposed into two components (i.e., background and gust velocity), Eq. (14) can be rewritten for a constant convective velocity vector as:

$$\frac{\partial\left(\tilde{u}_i + u_{g,i}\right)}{\partial t} + U_j^c\, \frac{\partial\left(\tilde{u}_i + u_{g,i}\right)}{\partial x_j} = 0. \tag{15}$$

Since SVM solves for the background velocity $\tilde{u}_i$, Eq. (15) is written for this variable as well:

$$\frac{\partial \tilde{u}_i}{\partial t} = -\left[\frac{\partial u_{g,i}}{\partial t} + U_j^c\, \frac{\partial\left(\tilde{u}_i + u_{g,i}\right)}{\partial x_j}\right]. \tag{16}$$

When no gust is introduced into the computational domain and the free-stream flow is directed in x-direction, the convective velocity vector is $U_j^c = [u_\infty,\ 0,\ 0]$, where u_∞ is the free-stream velocity. However, when a vertical gust is applied, a vertical convective velocity component is required to allow for the convection of mass in that direction. The most suitable physically sound choice is $U_j^c = [u_\infty,\ 0,\ w_{g,mean}]$, where $w_{g,mean}$ denotes the mean of the imposed gust velocity profile (i.e., $w_{g,mean} = \frac{A_g}{2}$).

Due to the fact that the third component of the gust velocity (i.e., $u_{g,3}$) is the only non-zero component in vertical gusts, the application of the convective boundary condition using Eq. (16) differs from the classical application in the vertical direction only. Moreover, since the gust velocity solely varies along the streamwise direction, its spatial derivative vanishes for all other directions. Expanding Eq. (16) for $\tilde{u}_3$ with the defined convective velocity vector reads:

$$\frac{\partial \tilde{u}_3}{\partial t} = -\left[\frac{\partial u_{g,3}}{\partial t} + u_\infty\, \frac{\partial\left(\tilde{u}_3 + u_{g,3}\right)}{\partial x_1} + w_{g,mean}\, \frac{\partial \tilde{u}_3}{\partial x_3}\right]. \tag{17}$$

Eq. (17) can be rearranged and written as:

$$\frac{\partial \tilde{u}_3}{\partial t} = -u_\infty\, \frac{\partial \tilde{u}_3}{\partial x_1} - w_{g,mean}\, \frac{\partial \tilde{u}_3}{\partial x_3} \underbrace{-\left[\frac{\partial u_{g,3}}{\partial t} + u_\infty\, \frac{\partial u_{g,3}}{\partial x_1}\right]}_{*}. \tag{18}$$

It is noticed that the term marked with $*$ is quite similar to the SVM source term in Eq. (11) except for the missing density and the free-stream velocity replacing the horizontal background velocity. Hence, this term proves to be essential for achieving the conservation of momentum when the convective boundary condition is prescribed in the context of the split velocity method. Note that the corresponding *-term in the equation for $\tilde{u}_1$ and $\tilde{u}_2$ is zero.

3. Numerical framework

3.1. Flow solver

The fully parallelized in-house finite-volume Navier–Stokes solver FASTEST-3D (Durst and Schäfer, 1996) is employed to solve for the incompressible fluid flow. The governing equations are discretized on a curvilinear, block-structured body-fitted grid with a collocated variable arrangement. The surface and volume integrals are approximated by the midpoint rule and the required flow variables at cell faces are linearly interpolated from neighboring cell-centered values leading to a second-order spatial accuracy. The time integration of the momentum equations is carried out using a second-order low-storage multi-stage Runge–Kutta method to obtain a provisional velocity. This predictor step yields an intermediate velocity field violating the continuity equation. Therefore, a Poisson equation for the pressure correction is solved and the coupled flow variables (i.e., velocities and pressure) are projected to the space of divergence-free vector fields in the so-called corrector step. This projection method (also known as predictor–corrector method) delivers velocities satisfying the mass conservation equation with a predefined accuracy (Breuer et al., 2012). Like in De Nayer et al. (2020), the large-eddy simulation (LES) technique is used to only resolve the large-scale turbulent flow field and model the small scales by a subgrid-scale (SGS) model. The standard Smagorinsky SGS model (Smagorinsky, 1963) with the well established constant $C_S = 0.1$ and van-Driest damping near solid walls is applied as it was shown to deliver reasonable results in De Nayer et al. (2018b).

In order to account for the multiphysics nature of a moving airfoil, the partitioned FSI approach presented in Breuer et al. (2012) is used to couple the fluid and the rigid-body solver. Moreover, the ALE formulation is used to account for two issues, namely, the time-dependent computational grid associated with the FSI problem and the pseudo-grid movement associated with the split velocity method. As the scope of this study is to investigate gust initiated airfoil oscillations, it is likely that the airfoil would undergo large translational and rotational movements. For this purpose, the hybrid grid adaption algorithm (IDW-TFI) developed by Sen et al. (2017) and particularly proposed for FSI-LES applications is used. This hybrid algorithm relies on two interpolation techniques, namely, the inverse distance weighting (IDW) interpolation for the block boundaries of the block-structured grid and a three-dimensional transfinite interpolation (TFI) for the inner grid points. The algorithm was found to be favorable as it combines two essential attributes, i.e., it retains the orthogonality of the grid in the vicinity of the moving body while maintaining acceptable CPU-time requirements. In the last decade this solver was intensively enhanced, tested and validated relying on complementary experimental and numerical pure CFD as well as FSI applications. With special focus on massively separated flows the following validation studies have to be mentioned.

In De Nayer et al. (2014) a complementary experimental–numerical investigation was carried out for the flow past a cylinder with a flexible splitter plate. The experimental setup was especially designed to be used as a well-defined but nevertheless challenging validation test case for fluid–structure interaction in turbulent flows. A detailed experimental investigation in a water tunnel using optical measurement techniques for both, the fluid flow and the structure deformation, were carried out and compared to LES predictions relying on the flow solver applied in the current study. The results were found to be in close agreement showing a quasi-periodic oscillating flexible structure in the first swiveling mode behind the bluff body. In Kalmbach and Breuer (2013) a second generic experimental FSI benchmark case was setup for a bluff-body flow combined with a flexible structure oscillating in the second swiveling mode. Again an enormous amount of flow field data as well as for the displacement of the structure were made available, which were used in De Nayer and Breuer (2014) to further validate the numerical methodology. The simulated phase-averaged data were found to be in close agreement with the experimental measurements concerning the form and the extrema of the deformation. Moreover, the frequency of the FSI phenomenon was well predicted with an error of less than 2.5%. Concerning other massively separated flows the complementary study by Wood et al. (2016) on the turbulent flow past a wall-mounted hemisphere (Re = 50,000) has to be mentioned. Here the flow detaches from the curved surface of the structure leading to extensive separations in the wake region comparable to the flow around airfoils at very high angles of attack. Comprehensive laser-Doppler measurements were conducted in a wind tunnel and compared with large-eddy simulations based on the present CFD code to validate the numerical simulations. Again the results of the measurements were found to be in close agreement with the predictions. Directly related to flows around airfoils are the combined studies of Wood et al. (2020) and De Nayer et al. (2020) which are the starting point of the current investigation. Here the flow around an elastically mounted NACA 0012 airfoil with two degrees of freedom was studied for different setups including large-amplitude oscillations and even flutter. Based on the numerical methodology also applied in the present study both limit-cycle oscillations and the flutter phenomenon yielding very high angles of attack could be reproduced by the coupled FSI predictions. For further validation studies, see Wood et al. (2018), De Nayer et al. (2018a), and Apostolatos et al. (2019).

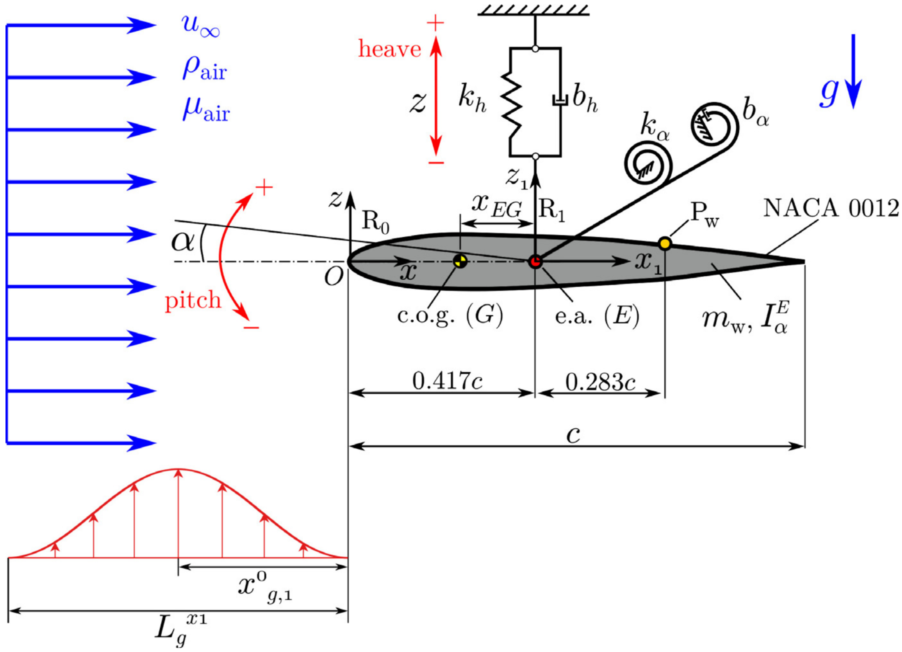

Fig. 2. Schematic representation of the investigated FSI case with all relevant parameters (notations from Wood et al. (2020)) and the introduced vertical gust velocity profile.

3.2. Rigid-body solver

The present FSI application is built on the precursor study of De Nayer et al. (2020) where the airfoil is treated as a rigid, but elastically mounted body (see Fig. 2). Consequently, fluid forces acting on the airfoil will cause its displacement as a single body without undergoing any structural deformations. In order to solve the dynamics of the airfoil experiencing fluid forces and moments, a solver describing the movement of the rigid body is applied. For this purpose, Newton's second law is considered in the Cartesian basis $R_0 = (x, y, z)$ for the translational and rotational motions, respectively. Leroyer and Visonneau (2005) wrote these equations in the form of a coupled system for the general case considering a moving deformable body. For the sake of brevity, only the necessary definitions, assumptions, and the resulting simplified equations are stated here (see De Nayer et al. (2020) for a detailed description). The airfoil has a local Cartesian coordinate system CCS (R_1) fixed to its elastic axis (e.a. or E). The governing equations for the rotational motions are written for this coordinate system. Therefore, the mass moment of inertia matrix is diagonal and time-independent. Moreover, the equations for the translational motion are formulated for the center of gravity denoted c.o.g. or G. Since the setup has only two degrees of freedom (2-DOF), i.e., translation in the z-direction and rotation around the y-axis, the system of equations describing the motion is reduced to two equations. This cancels out all other DOFs and their contributions to the inertial source terms. In fact, for the rigid airfoil considered, only a single source term associated with the heave DOF and arising from the rigid-body rotation remains.

The simplified coupled system of equations employed reads:

$$\begin{aligned} &m_w\,\ddot{z} + b_h\,\dot{z} + k_h\,z - \underbrace{x_{EG}\,m_w}_{*}\,\ddot{\alpha} = F_{\text{CFD},3} - \underbrace{\left(-m_w\,\dot{\alpha}^2\,z_{EG}\right)}_{S_{R,3}} \quad , \\ &I^E_\alpha\,\ddot{\alpha} + b_\alpha\,\dot{\alpha} + k_\alpha\,\alpha - \underbrace{x_{EG}\,m_w}_{*}\,\ddot{z} = M_{\text{CFD},2} \quad , \end{aligned} \tag{19}$$

where z denotes the heave DOF, α the pitch DOF, b_h and b_α the material damping coefficients of the respective DOF and k_h and k_α the material stiffnesses of the respective DOF. m_w and I^E_α are the airfoil's mass and the mass moment of inertia regarding the elastic axis E. $F_{\text{CFD},3}$ is the lift force and $M_{\text{CFD},2}$ denotes the moment due to the fluid flow evaluated with respect to the elastic axis E. x_{EG} and z_{EG} are the horizontal and the vertical distance between E and G, respectively. The term marked with $*$ is the so-called "static moment" and $S_{R,3}$ is the aforementioned source term. Both act as coupling terms between the heave and pitch motions.

It is worth mentioning that in order to circumvent potential singularities during the computation of the rotational DOF, Euler angles are replaced by *quaternions* as used in Leroyer and Visonneau (2005). In the present partitioned approach,

Table 1
Mechanical parameters of the coupled system.

Parameter	Symbol	Unit	Value
Distance between c.o.g. and e.a. (x_{EG})	x_{EG}/c	–	0.006
Mass of dynamic system	m_{w}	kg	0.33521
Mass moment of inertia based on $f_{\alpha}^{\text{1-DOF}}$	I_{α}^{E}	kg m^2	1.381×10^{-4}
Bending stiffness	k_h	N/m	705
Torsional stiffness	k_{α}	Nm/rad	0.3832
Translational material damping ratio	D_h	–	2.30×10^{-3}
Rotational material damping ratio	D_{α}	–	1.15×10^{-3}

the time-step size is identical for the fluid and structural solvers. To obtain the solution of the motion at a new time step $n+1$, the coupled system in Eq. (19) is solved sequentially, since the time step used by LES is very small. The static moment terms are moved to the right-hand side and taken from the previous time step n:

$$\begin{aligned} m_w\, \ddot{z}^{n+1} + b_h\, \dot{z}^{n+1} + k_h\, z^{n+1} &= F_{\text{CFD, 3}}{}^{n+1} + x_{EG}^{n}\, m_w\, \ddot{\alpha}^{n} + z_{EG}^{n}\, m_w\, \left(\dot{\alpha}^{n}\right)^2 \quad , \\ I_{\alpha}^{E}\, \ddot{\alpha}^{n+1} + b_{\alpha}\, \dot{\alpha}^{n+1} + k_{\alpha}\, \alpha^{n+1} &= M_{\text{CFD, 2}}{}^{n+1} + x_{EG}^{n}\, m_w\, \ddot{z}^{n} \quad . \end{aligned} \tag{20}$$

The temporal discretization of the system of Eqs. (20) is implemented by using the *standard Newmark* method of second-order accuracy in time (Newmark, 1959). The Newmark parameters are set to $\beta = 0.25$ and $\gamma = 0.5$.

3.3. Coupling scheme

For the partitioned approach applied an exchange between both solvers is required. For this purpose, the pressure and shear forces on the airfoil are integrated up to determine the resulting force $F_{\text{CFD, 3}}$ and moment $M_{\text{CFD, 2}}$. At each time step these values are transferred to the rigid-body solver. In the other direction the structural displacements of the surface obtained by the superposition of the z-translation and the rotation around the y-axis are imposed at each fluid node of the FSI interface. An additional first-order estimation of the displacements at the beginning of each time step was found to be advantageous. The displacements of the surface of the airfoil are the input parameter for the grid adaption described in Section 3.1. Since in the present application the added-mass effect is negligible, a loose coupling algorithm is preferred. It delivers highly reliable results and saves a huge amount of CPU time in comparison to predictions based on a strong coupling scheme (De Nayer et al., 2020).

4. Description of the FSI case

The FSI case consists of an elastically mounted NACA 0012 airfoil of a chord length $c = 0.1$ m undergoing heave and pitch motions inspired by the experimental work of Wood et al. (2020) and the numerical counterpart by De Nayer et al. (2020). The airfoil is exposed to a constant free-stream velocity u_{∞} and vertical gravity $\vec{g} = -g\, \vec{e}_z$ as sketched in Fig. 2. The wing which is initially at an angle of attack of 0° is allowed to pitch around its elastic axis located at a distance of $c_E = 0.417c$ from the leading edge. It is assumed that the structural setup can be modeled by a mass–spring–damper system for both degrees of freedom. Hence, six structural parameters are necessary to fully define the system. These parameters are the coefficients of Eq. (20) (i.e., m_{w}, I_{α}^{E}, k_h, k_{α}, $b_h = 2D_h\sqrt{k_h m_{\mathrm{w}}}$ and $b_{\alpha} = 2D_{\alpha}\sqrt{k_{\alpha} I_{\alpha}^{E}}$). The mechanical properties used in the current study are those determined in De Nayer et al. (2020) for configuration **I**, in which the center of gravity nearly coincides with the center of rotation (i.e., $x_{EG} \approx 0$). In this configuration, the equations of motion (i.e., Eq. (20)) are almost uncoupled (in terms of inertia). Beside this setup two alternative configurations (**II** and **III**) were considered in these precursor studies mainly differing by the distance between the center of gravity and the center of rotation, i.e., $x_{EG} < 0$ and $x_{EG} > 0$. As shown in Wood et al. (2020) and De Nayer and Breuer (2020) the distance x_{EG} alters the dynamic characteristics of the system and is therefore an interesting parameter to study limit-cycle oscillations and flutter. Since most numerical simulations were carried out for case **I** and the system is considered to possess a higher stability compared to the case with $x_{EG} > 0$, which makes it more challenging with regard to the possible excitation by wind gusts, this configuration was chosen in the present study.

The parameters used are summarized in Table 1. The fluid properties defined are those of air at a constant temperature ($T = 288$ K) where the density and dynamic viscosity are $\rho_{\text{air}} = 1.225$ kg/m^3 and $\mu_{\text{air}} = 18.27 \times 10^{-6}$ Pa s, respectively. For all cases studied, a constant free-stream velocity of $u_{\infty} = 5.06$ m/s is set yielding a Reynolds number $\mathrm{Re} = \rho_{\text{air}}\, u_{\infty}\, c/\mu_{\text{air}} = 33,900$. In Wood et al. (2020) and De Nayer et al. (2020) this setup was investigated for a wide range of transitional Reynolds numbers ($9.66 \times 10^3 \leq \mathrm{Re} \leq 3.60 \times 10^4$). While the overall kinematic state of the system was strongly damped for low Reynolds numbers, it got constantly amplified for the highest Reynolds number (i.e., flutter phenomenon). Within the range of Re = 33,900, the authors found the airfoil to be undergoing a series of sustained bounded amplitude oscillations with moderate angles upon the application of an external perturbation. Therefore, this Reynolds number is employed in the present study. Unlike the procedure followed in De Nayer et al. (2020), where the airfoil was initially excited by mechanical perturbations (initially prescribed lift force and pitching moment), this

Table 2
Vertical gust characteristics.

g_1	$f_t(t)$	$f_1(\xi)$	$f_2(\eta)$	$f_3(\zeta)$	$L_g^{x_1}/c$	$x_{g,1}^0/c$	A_g/u_∞		
e_3					2	−1	1	2	3
e_3	1	1	ECG	1	4	−2	1	2	3
e_3					6	−3	1	2	3

work aims to study the gust-induced perturbations and their effect on the airfoil's stability. Therefore, vertical wind gusts introduced upstream of the airfoil and convected downstream with a horizontal velocity $u_{g,conv} = u_\infty$ are used for this purpose. Gusts of different lengths (i.e., $L_g^{x_1}$) and several amplitudes (i.e., A_g) are investigated. The gust center coordinate (i.e., $x_{g,1}^0$) is chosen such that the leading edge of the gust and the airfoil coincide as shown in Fig. 2. The gust characteristics of the simulations performed are summarized in Table 2.

Considering commercial aircrafts operating at a cruise speed in the order of Mach number Ma $= 0.8$, the typical gust ratios relevant for this situation (defined by the certification rules of the European Aviation Safety Agency or the Federal Aviation Administration) are at least one order of magnitude smaller than those taken into account here. Nevertheless, high gust ratios make sense for Micro-Air Vehicles (MAVs), which are small aircrafts operating either remotely or autonomously at low flight velocities and thus moderate Reynolds numbers in the range considered in the present study. Here the gust response is a fundamental problem decisive for flight stability, maneuverability and control of MAVs. A recent study by Poudel et al. (2021) provides an interesting literature overview on the topic of gusts interacting with MAVs and motivates the necessity to study nonlinear, high magnitude gust-wing interactions. Other studies also considering large gust ratios are for example provided by Andreu-Angulo et al. (2020) and Perrotta and Jones (2017).

The computational domain around the NACA 0012 airfoil depicted in Fig. 3(a) is an extended version of that applied in the preceding study (De Nayer et al., 2020). The C-type grid of the inner domain (marked by black lines) is kept unchanged but extended in the radial direction (with r_{ex}) and in the wake of the airfoil (with w_{ex}). The extended sections have equidistant control volumes of cell heights identical to the respective last cell of the inner domain. This extension of the computational domain is intended to provide more space for the vortical structures resulting from the airfoil–gust interaction to develop above and past the airfoil. The extent of the flow domain is justified by previous investigations of similar flow cases, c.f. Breuer (2018) and the references cited therein. The radius of the semi-cylinder is now $\mathrm{r}_{tot} = \mathrm{r} + \mathrm{r}_{ex} = (7.2 + 4.1)c = 11.3\,c$, the wake length is $\mathrm{w}_{tot} = \mathrm{w} + \mathrm{w}_{ex} = (5 + 7)c = 12\,c$.

A critical issue for this kind of geometrically two-dimensional airfoils is the appropriate choice of the spanwise extension of the computational domain. Following the considerations in Schmidt and Breuer (2014, 2017) the width of the domain is set to $l_c = 0.25\,c$. According to Breuer (2018) this is a compromise between spanwise extension and spanwise resolution and based on grids of other research groups, e.g., Galbraith and Visbal (2009) and Visbal et al. (2009) with spanwise extensions of $l_c = 0.1$–$0.3\,c$. Galbraith and Visbal (2009) found only marginal differences between the different cases. Furthermore, Schmidt (2016) carried out additional simulations with a doubled spanwise domain size ($l_c = 0.5\,c$) evaluating two-point correlations. These investigations confirm the present choice. Note that these reference cases were carried out for flows in the same Reynolds number range. For flows at significantly higher Re $= \mathcal{O}(10^6)$ even much smaller spanwise extensions ($l_c/c = 0.012 - 0.06$) are typically used, see, e.g., Mellen et al. (2003) and Lobo et al. (2022).

The grid consists of 1,878,720 control volumes (CVs) and 60 CVs are equidistantly distributed in the spanwise direction. The distance between the first cell center and the wall in wall-normal direction is 4×10^{-5} m with a geometrical stretching factor in the wall-normal direction of $q_s = 1.1$. A zoom of the grid in the vicinity of the airfoil is shown in Fig. 3(b). With this setup the viscous sublayer can be resolved and thus no-slip conditions are used on the surface of the airfoil. In order to prove this statement, additional LES predictions were carried out for the flow around the fixed airfoil at angles of attack in the range $0 \leq \alpha \leq 80°$. In the Appendix these simulations are evaluated depicting the y^+ values of the wall-nearest grid points on the suction and pressure side of the airfoil. Obviously, at most points on the suction side the y^+ values are below unity. On the pressure side the values are slightly higher but even the peak values are below $y^+ = 5$. Thus, the dimensionless wall distance is in the range which allows to resolve the viscous sublayer.

Fig. 3(a) depicts the definition of the boundary conditions of the computational domain. At the inlet and the bottom boundary a constant free-stream velocity u_∞ is assumed, which means that the turbulence intensity is set to zero in order to concentrate on the effect of the wind gust on the airfoil behavior. Furthermore, in the spanwise direction periodic boundary conditions are applied. At the outlet and the top boundary a convective outflow boundary condition is prescribed as explained in Section 2.3.

To ensure the stability of the explicit time integration scheme used in the predictor step (see Section 3.1), a dimensionless time-step size of $\Delta t\, u_\infty/c = 5.06 \times 10^{-4}$ is applied. That corresponds to a maximum CFL number of about 0.5 and thus guarantees that the flow structures resolved in space by LES are also appropriately resolved in time.

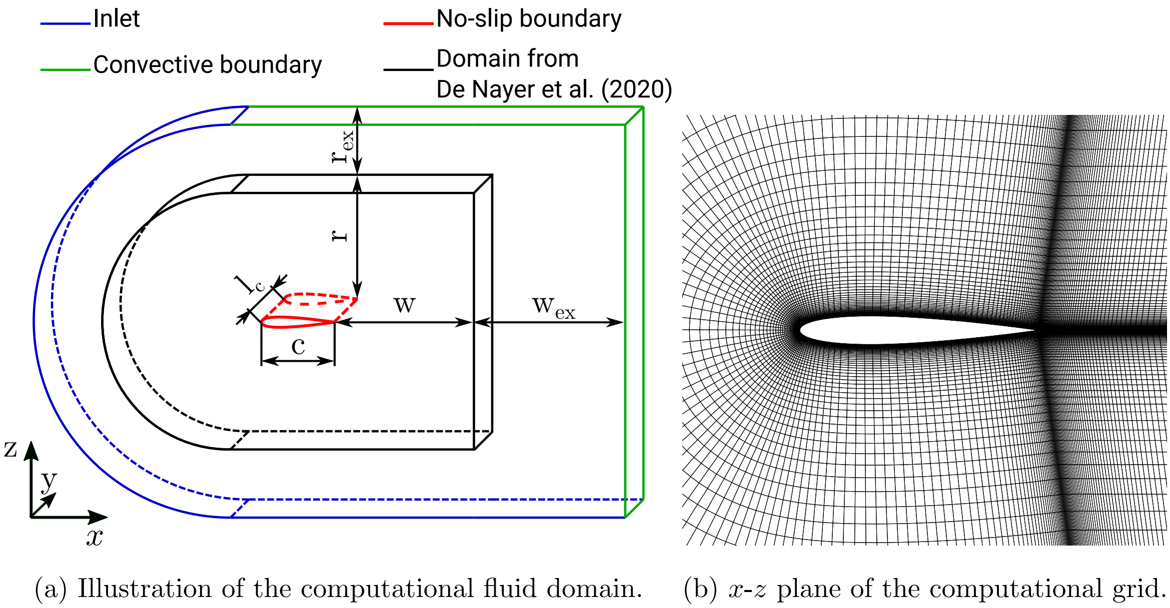

Fig. 3. CFD setup.

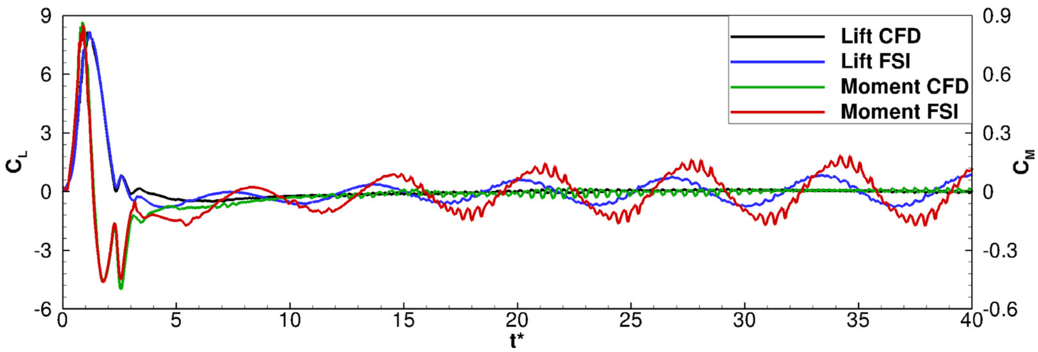

Fig. 4. Instantaneous lift and pitching moment coefficients of a fixed (CFD) and an elastically mounted airfoil (FSI) when subjected to a vertical gust of length $L_g^{x_1}/c = 2$ and amplitude $A_g/u_\infty = 2$. The sign definition is according to Fig. 2, i.e., the lift is positive in z-direction and the moment is positive in clockwise direction. (For interpretation of the references to colour in this figure legend, the reader is referred to the web version of this article.)

5. Results

5.1. CFD vs. FSI case

First results compare the aerodynamic forces exerted on the airfoil between two cases, namely, a fixed airfoil (CFD) and an elastically mounted airfoil (FSI). Fig. 4 depicts the instantaneous lift and pitching moment coefficients of the airfoil encountering a 1-cosine vertical gust of length $L_g^{x_1}/c = 2$ and strength $A_g/u_\infty = 2$. At $t^* = 0$ (where $t^* = u_\infty t/c$) the airfoil's leading edge starts penetrating the gust yielding an increase in the lift and the pitching moment coefficients. While the rise in the lift coefficient is attributed to an increase in the effective angle of attack of the airfoil, that of the pitching moment coefficient is due to the generated clockwise moment. This moment is a consequence of the high and low pressure fields acting concurrently to the left of the elastic axis on the airfoil's upper and lower surfaces, respectively (see pressure field snapshots at $t^* = 1$ in Figs. 5 and 6). During this phase of interaction a clockwise rotating leading-edge vortex (LEV) is formed. Obviously, the pressure and velocity distributions are quasi identical for the fixed and the elastically mounted airfoil at this instant in time. Since both the heave and the pitch motion are still very small at this early stage, the marginal deviations between both cases can be explained.

The steady increase in the magnitude of both coefficients continues until peak values at different instants in time are reached. While the pitching moment coefficient records its maximum magnitude when the gust center reaches the vicinity of the leading edge ($t^* \approx 0.9$), the peak of the lift occurs when the gust center is shortly behind the leading edge

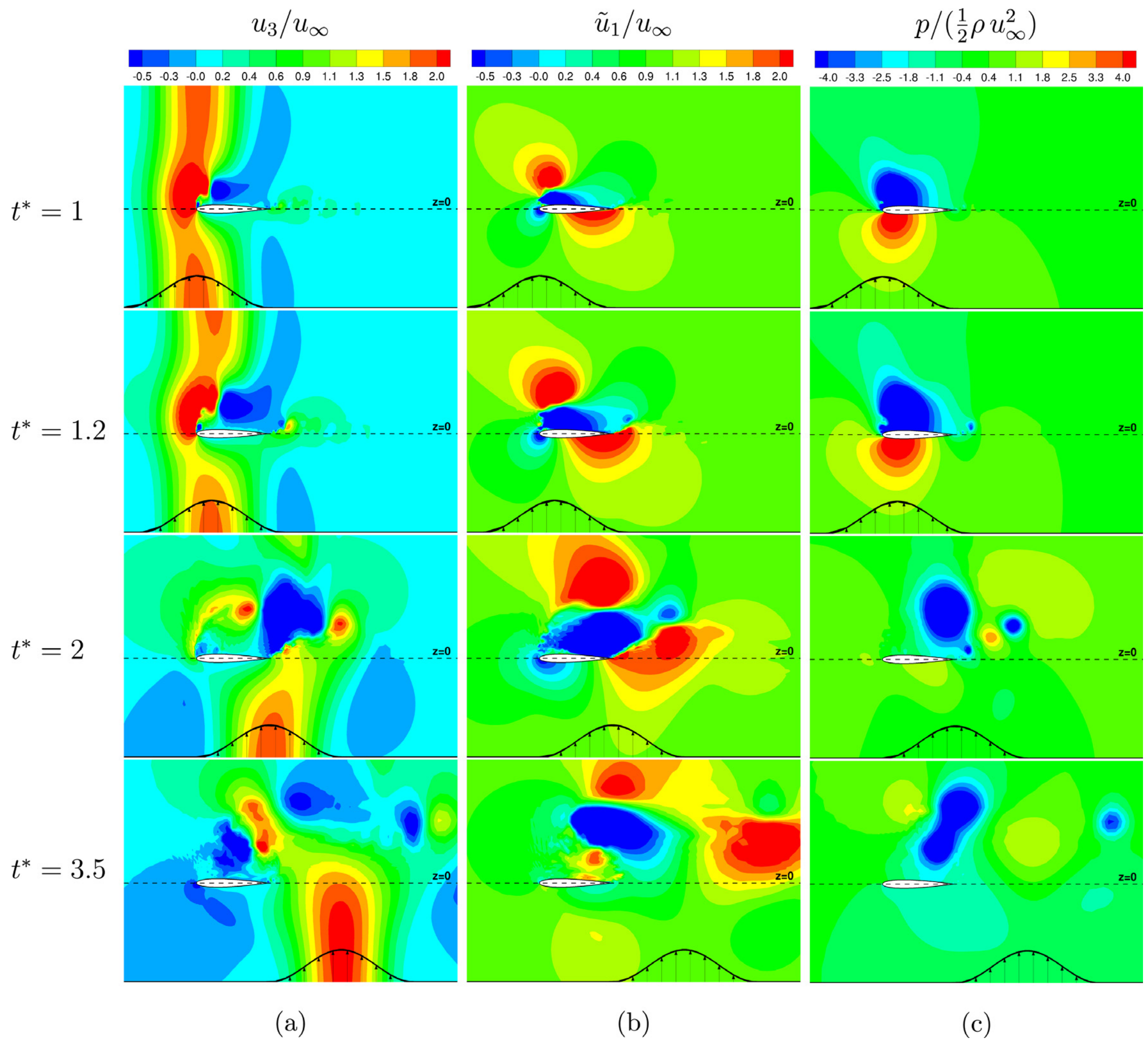

Fig. 5. Snapshots of the total vertical velocity (a), the background streamwise velocity (b) and the pressure (c) fields of the gust encounter ($L_g^{x_1}/c = 2$, $A_g/u_\infty = 2$) on the fixed airfoil. $t^* = 1$: gust at leading edge, $t^* = 1.2$: instant at maximum lift, $t^* = 2$: gust center at trailing edge, $t^* = 3.5$: gust completely left the airfoil.

and before the mid-chord ($t^* \approx 1.2$ in Figs. 5 and 6). Again the deviations in the flow fields of the fixed and the elastically mounted airfoil are marginal. This can be explained with the same argument as before.

The lift coefficient then starts decaying to eventually recover the level of the steady-state values when the gust has completely left the plate. On the other hand, the pitching moment coefficient experiences a decrease to negative values as the gust center and the leading-edge vortex travel downstream along the chord of the airfoil (i.e., for $0.9 \leq t^* \leq 2.5$ as shown in Fig. 4). Although nearly identical histories are obtained during the airfoil–gust interaction (i.e., until $t^* = 3$) and thus the velocity and pressure fields in Figs. 5 and 6 are still in close agreement, the curves of the FSI case continue to oscillate (see discussion on limit-cycle oscillations in Section 5.3) while their CFD counterparts recover to the quasi steady-state values. Oscillating aerodynamic forces contribute to dampening as well as to amplifying the motion as found in later investigations. At the last instant in time ($t^* = 3.5$) depicted in Figs. 5 and 6 some small deviations in the resulting flow fields can be detected which are due to the induced onset of the pitch and heave motion.

The high-frequency components in the lift and moment coefficients, which in the FSI case are superimposed on the motion-dominated low-frequency components for $t^* > 10$, are the result of the laminar flow separation from the airfoil's lower and upper surface. To investigate this phenomenon, the spanwise y-vorticity ω_y (plotted on a mid-span slice), the skin-friction coefficient C_f (plotted on the upper surface of the airfoil), and the location of flow separation are depicted for different time instants in Fig. 7. The instants at which the snapshots (i.e., snapshots a–h) are taken correspond to the points in Fig. 8 showing the respective heave and pitch angle values. The snapshots depicted in Fig. 7a to d clearly show that when the airfoil starts to pitch up reaching its maximum angle of attack, the separation starting in the vicinity of

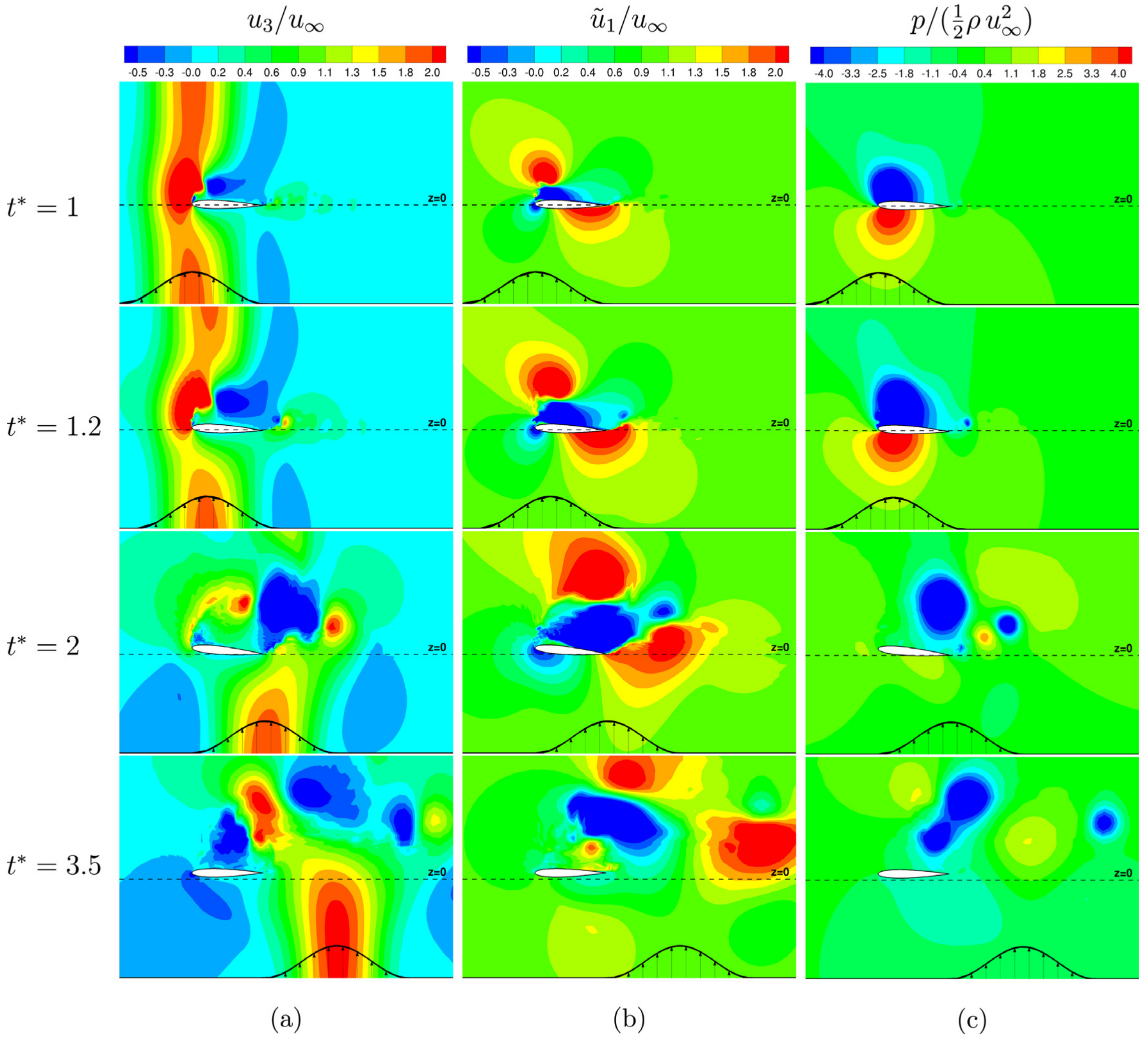

Fig. 6. Snapshots of the total vertical velocity (a), the background streamwise velocity (b) and the pressure (c) fields of the gust encounter ($L_g^{x_1}/c = 2$, $A_g/u_\infty = 2$) on the elastically mounted airfoil. $t^* = 1$: gust at leading edge, $t^* = 1.2$: instant at maximum lift, $t^* = 2$: gust center at trailing edge, $t^* = 3.5$: gust completely left the airfoil.

the trailing edge moves upstream on the suction side. During the phase when the angle of attack is already decreasing again, vortices are shed from the suction side (see Fig. 7f and g). These vortices disappear when the angle of attack tends towards the other extremum (see Fig. 7h) and thus a favorable pressure gradient occurs on the corresponding side of the airfoil. At that stage the same process begins on the lower surface. Note that the flow phenomena described above are mostly two-dimensional which is typical for a laminar flow separation. The separated shear layers become unstable further downstream leading to the development of three-dimensional structures and later to the transition to turbulence. That explains the spanwise varying separation line visible in Fig. 7h.

Although similar high-frequency components are observed in the fixed case, those are rather caused by the continuous vortex-shedding process observed close to the trailing edge. Consequently, the phenomenon appears independent of the gust, but is augmented by the gust due to the resulting motion and especially the increase in the angle of attack.

5.2. Effect of the gust strength on the FSI case

As mentioned in Section 4, the effect of gust-induced perturbations on the dynamic behavior of the elastically mounted airfoil is intended to be studied. For that reason, a series of FSI simulations is carried out to investigate the influence of different gust strengths (at a fixed gust length) on the aeroelastic response of the airfoil. The time histories of the instantaneous dimensionless heave and pitch of the airfoil exposed to vertical gusts of the gust length $L_g^{x_1}/c = 2$ (see Table 2) are depicted in Fig. 9.

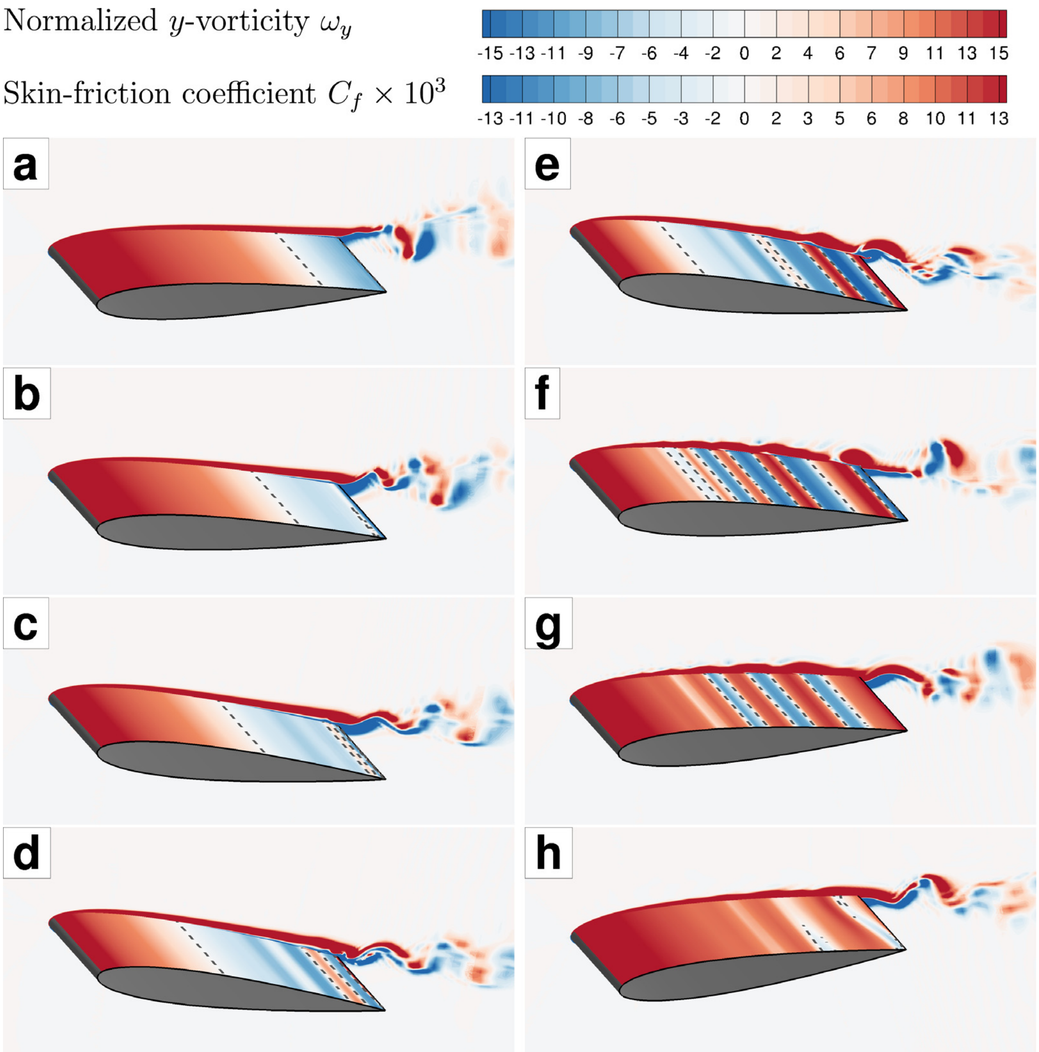

Fig. 7. Normalized y-vorticity ω_y (on the mid-span slice), skin-friction coefficient C_f (on the upper surface of the airfoil), and separation location (dashed line) for eight time instants (a–h) corresponding to the instants given in Fig. 8.

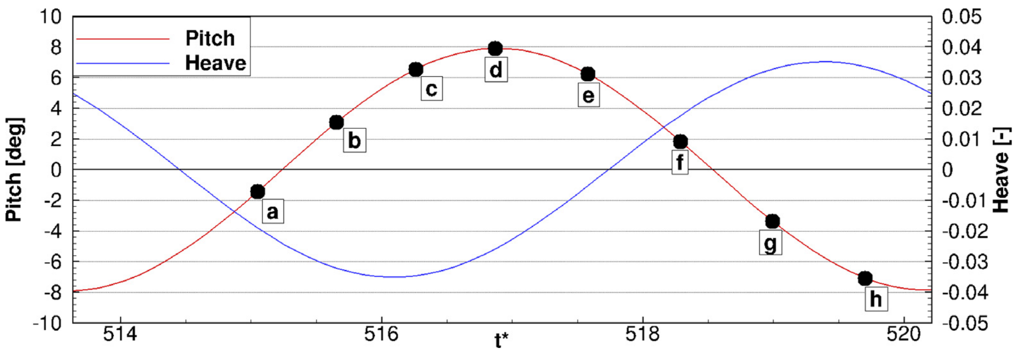

Fig. 8. Pitch angle and heave DOF during a LCO cycle.

A sudden increase in the magnitude of the heave and pitch as a reaction to the gust-imposed lift and pitching moment (depicted in Figs. 9(c) and 9(g), respectively) is observed for all three gust strengths. Especially the initial heave excitation strongly depends on A_g, whereas the first peak of the pitch marginally is nearly identical for all gust strengths. Pitch

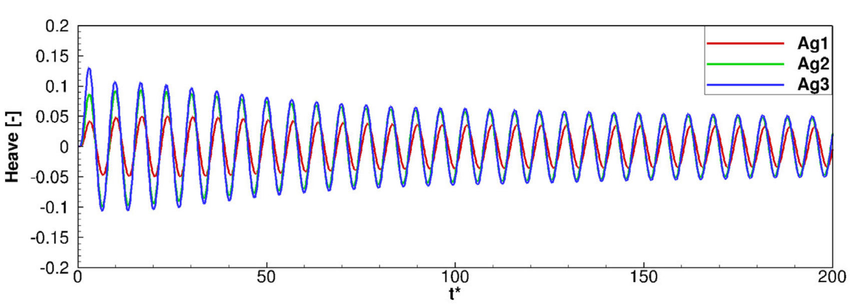

(a) Heave DOF for $L_g^{x_1}/c = 2$.

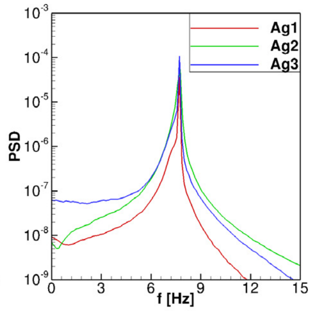

(b) FFT.

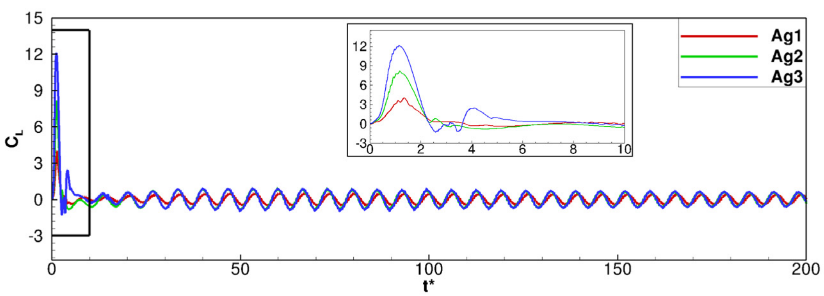

(c) Lift coefficient for $L_g^{x_1}/c = 2$.

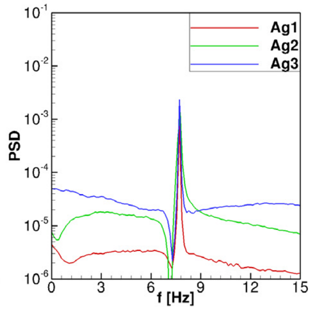

(d) FFT.

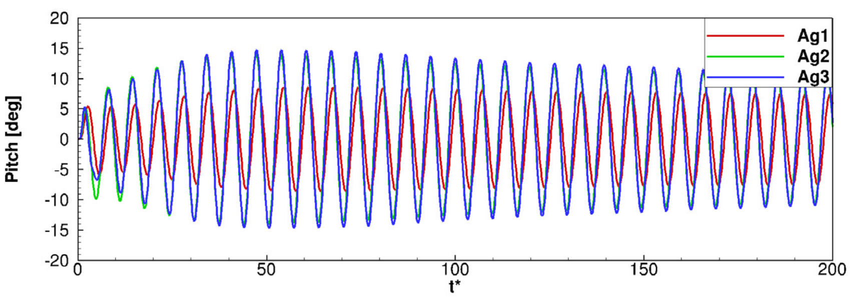

(e) Pitch DOF for $L_g^{x_1}/c = 2$.

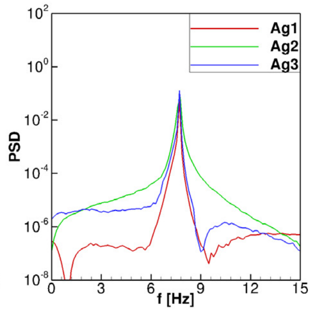

(f) FFT.

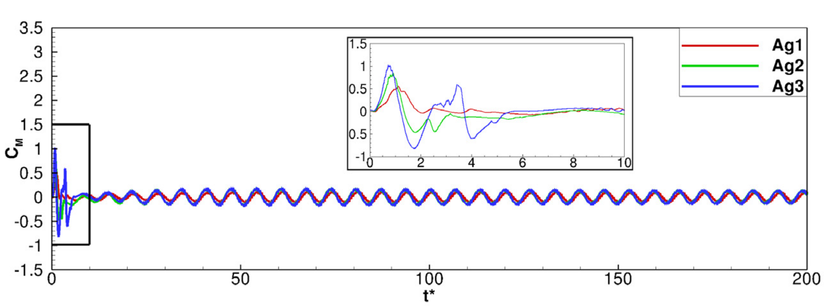

(g) Pitching moment coefficient for $L_g^{x_1}/c = 2$.

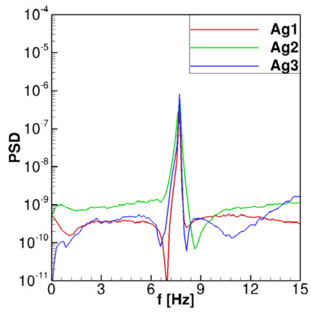

(h) FFT.

Fig. 9. Instantaneous heave and pitch DOFs (a,e), lift and pitching moment coefficients (c,g) of the elastically mounted airfoil when subjected to vertical gusts of length $L_g^{x_1}/c = 2$ at three gust strengths $A_g/u_\infty = 1, 2$ and 3.

Table 3
Oscillation frequencies associated with the elastically mounted airfoil subjected to different vertical gusts. The cases in which flutter occurs, are given in boldface.

$L_g^{x_1}/c$	–	2			4			6		
A_g/u_∞	–	1	2	3	1	2	**3**	1	2	**3**
Heave frequency	[Hz]	7.70	7.75	7.70	7.63	7.63	**7.81**	7.66	7.68	**7.92**
Pitch frequency	[Hz]	7.70	7.75	7.70	7.63	7.63	**8.10**	7.66	7.68	**7.92**
Lift frequency	[Hz]	7.70	7.75	7.70	7.63	7.63	**7.81**	7.66	7.68	**7.92**
Moment frequency	[Hz]	7.70	7.75	7.70	7.63	7.63	**8.10**	7.66	7.68	**7.92**
Phase angle	deg	135.2	138.6	138.9	138.3	140.8	162.8	138.4	139.3	–

oscillations continue to gain amplitude until $t^* \approx 54$ (i.e., the 9th cycle) for all prescribed gust strengths. The oscillations then start to steadily decay finally arriving at a bounded amplitude (i.e., a limit-cycle oscillation). For the heave DOF, a similar trend is observed for $A_g/u_\infty = 1$ and 2, where a maximum amplitude is reached at about $t^* = 16.7$ (i.e., the 3$^{\text{rd}}$ cycle). However, for the strongest gust (i.e., $A_g/u_\infty = 3$) the maximum heave amplitude is recorded within the first cycle and the oscillatory behavior is then seen to undergo a damped motion approaching the limit-cycle oscillation. Considering the aerodynamic forces it is found that the stronger the gust is, the higher are the lift and pitching moment coefficients observed. This is of course expected as stronger gusts induce higher aerodynamic forces and moments which describe the right-hand side of Eq. (19). Overall, a direct relationship between the gust strength and the maximum heave and pitch amplitudes reached during the gust impact and the immediate phase thereafter is also obvious. However, additional simulations continuing the present case far beyond $t^* > 200$ have provided clear evidence that the amplitudes of heave and pitch aim for the same final bounded values.

5.3. Effect of the gust length on the FSI case

The heave and pitch DOF responses of the further investigated gust lengths (i.e., $L_g^{x_1}/c = 4$ and $L_g^{x_1}/c = 6$) shown in Figs. 10 and 11 exhibit a similar tendency for gust strengths of $A_g/u_\infty = 1$ and 2. However, it is worth mentioning that for the same gust strength, wider gusts are found to cause higher amplitudes across the aerodynamic forces and their respective degrees of freedom during the gust encounter. This is expected as, for wider gusts, the airfoil experiences a higher effective angle of attack along its chord for a longer period of time. Again, both DOFs show an initial increase upon the gust encounter followed by a continuous decrease to eventually settle after several oscillation cycles at a stage of sustained bounded amplitudes. Note that in the long term the amplitudes observed for excitations by gusts of different length scales are identical for both gust strengths of $A_g/u_\infty = 1$ and 2. In accordance with the previously discussed case of $L_g^{x_1}/c = 2$ a limit-cycle oscillation is induced by the gusts of these strengths ($A_g/u_\infty \leq 2$).

In contrast, for a gust strength of $A_g/u_\infty = 3$ the prescribed gusts tend to induce significantly larger excitations which trigger a diverging pitch motion. While the amplitude of the heave oscillations experiences a steady decay (see $A_g/u_\infty = 3$ in Figs. 10(a) and 11(a)), the pitch DOF engages in a series of oscillations in which the amplitude is constantly increasing (see Figs. 10(e) and 11(e)). Obviously, these two cases do not show a limit-cycle oscillation anymore, but represent the flutter case. Except the heave motion the amplitudes of all other quantities (lift, pitch, pitching moment) continuously increase until finally the predictions could not be continued and blow up due to an overwhelming pitch motion. Thus, in case of an excitation by a strong wind gust ($A_g/u_\infty \geq 3$) with a sufficiently large length ($L_g^{x_1}/c \geq 4$) the flutter scenario can already be reached at Re = 33,900, whereas in the previous study of the identical configuration using artificial initial perturbations (De Nayer et al., 2020) the flutter case was only achieved at a higher Reynolds number of Re = 36,000.

Moreover, despite the preserved periodicity of the heave and pitch motion, the aerodynamic coefficients show more complex time histories which is the outcome of additional higher frequencies observed in the signals. A frequency analysis carried out for both DOFs along with their respective driving forces for all gust lengths and strengths is depicted on the right columns of Figs. 9 to 11. The frequencies corresponding to the maximum power spectral density of each case are summarized in Table 3. It can be observed that for all cases in which the system converges to the limit-cycle oscillation, all signals oscillate at nearly the same frequency. The frequency of oscillation varies slightly across these cases in a small range of (7.63, 7.75). That is at its maximum about 1.5% and the deviations are attributed to inaccuracies in determining the peak values. The dominant frequency is also in close agreement with the preceding study (De Nayer et al., 2020), in which a frequency of 7.69 Hz was determined for the oscillations with moderate amplitudes. However, for the cases in which flutter occurs, an increase in the frequency of oscillation of approximately 5% (especially for the pitch DOF) is found. Table 3 also provides the observed phase angles. For the LCO case the values predicted in the current study are in close agreement with the value of 138° found in De Nayer et al. (2020). In the flutter case the determination of the phase angle is more challenging. In accordance with the previous work, an increase of the phase angle is observed.

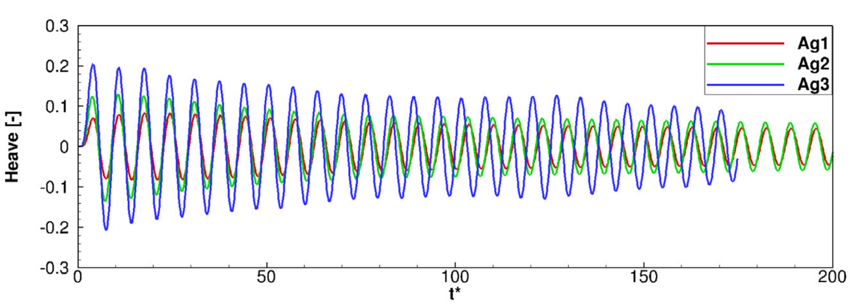

(a) Heave DOF for $L_g^{x_1}/c = 4$.

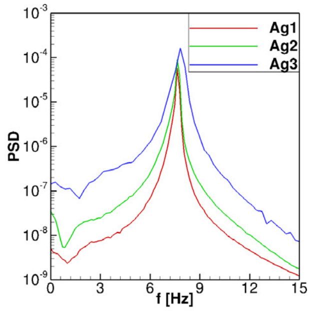

(b) FFT.

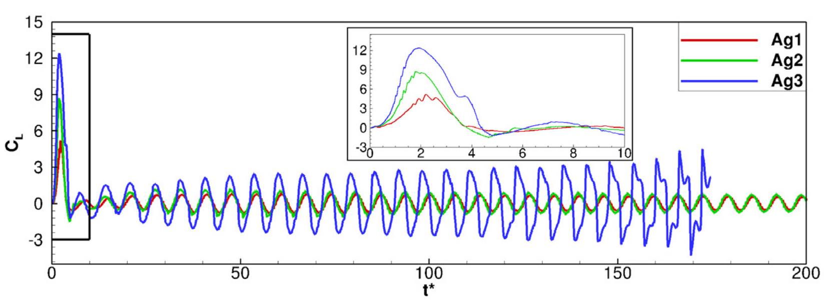

(c) Lift coefficient for $L_g^{x_1}/c = 4$.

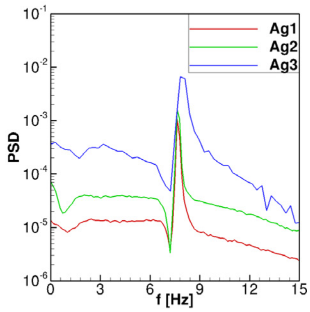

(d) FFT.

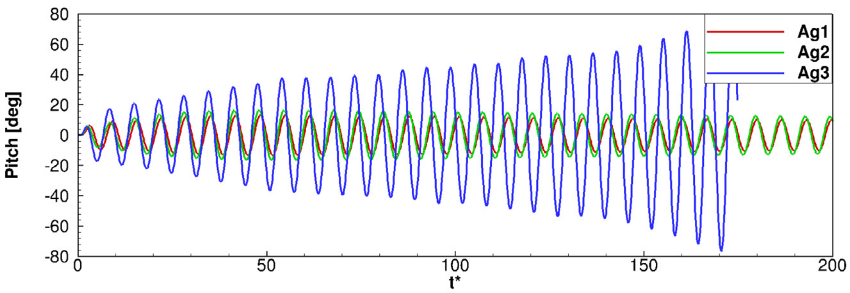

(e) Pitch DOF for $L_g^{x_1}/c = 4$.

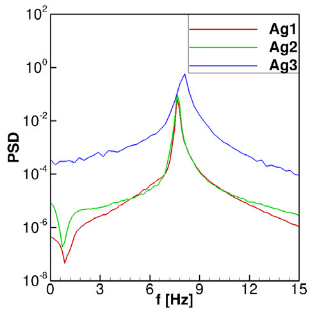

(f) FFT.

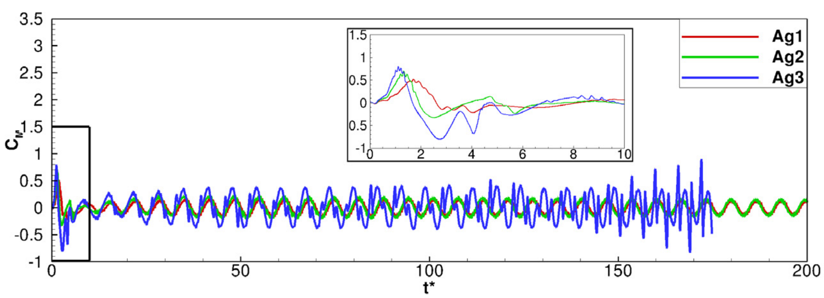

(g) Pitching moment coefficient for $L_g^{x_1}/c = 4$.

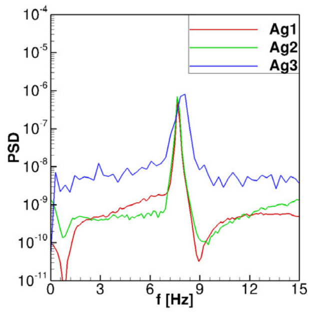

(h) FFT.

Fig. 10. Instantaneous heave and pitch DOFs (a,e), lift and pitching moment coefficients (c,g) of the elastically mounted airfoil when subjected to vertical gusts of length $L_g^{x_1}/c = 4$ at three gust strengths $A_g/u_\infty = 1, 2$ and 3.

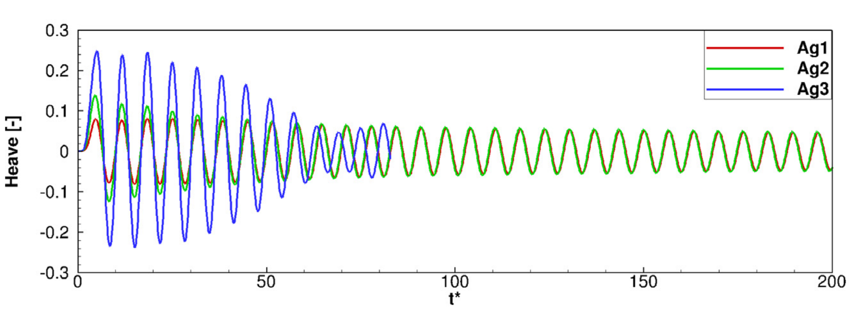

(a) Heave DOF for $L_g^{x_1}/c = 6$.

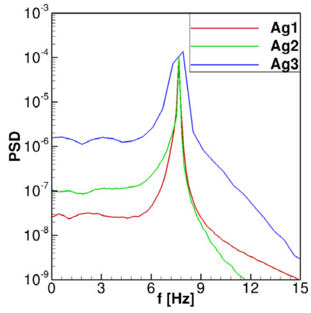

(b) FFT.

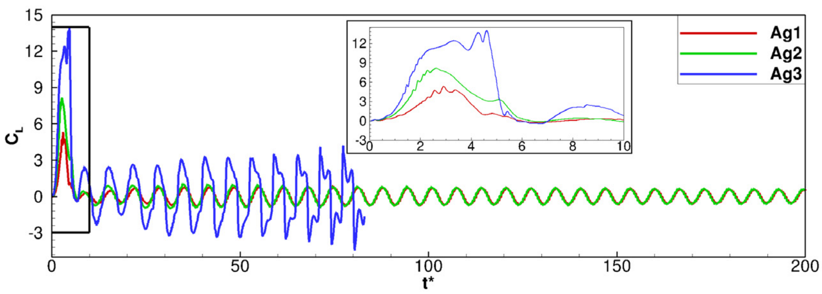

(c) Lift coefficient for $L_g^{x_1}/c = 6$.

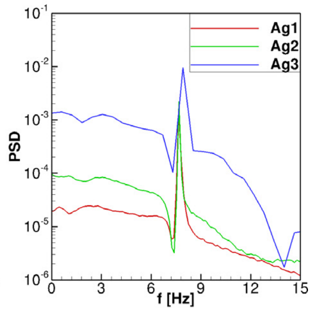

(d) FFT.

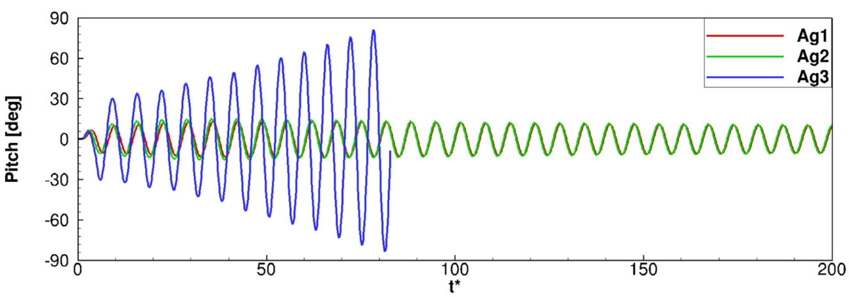

(e) Pitch DOF for $L_g^{x_1}/c = 6$.

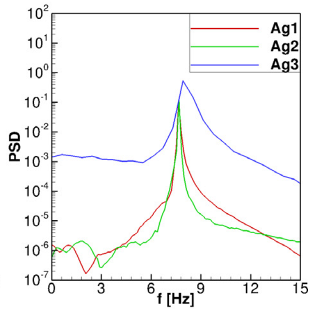

(f) FFT.

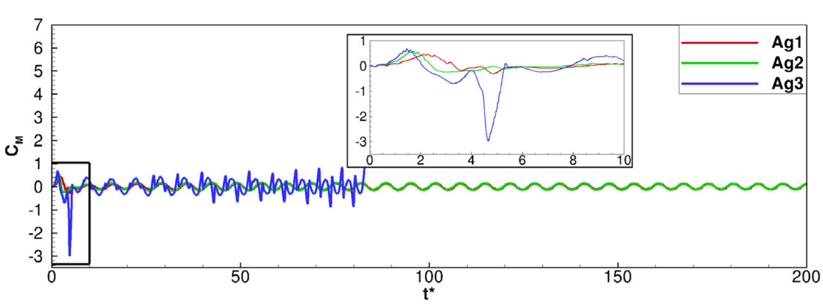

(g) Pitching moment coefficient for $L_g^{x_1}/c = 6$.

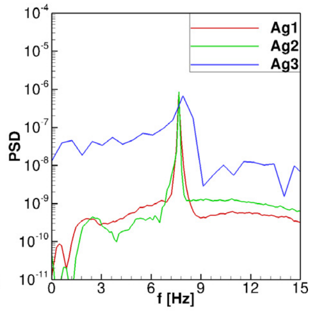

(h) FFT.

Fig. 11. Instantaneous heave and pitch DOFs (a,e), lift and pitching moment coefficients (c,g) of the elastically mounted airfoil when subjected to vertical gusts of length $L_g^{x_1}/c = 6$ at three gust strengths $A_g/u_\infty = 1, 2$ and 3.

5.4. LCO vs. flutter gust interaction

The y-vorticity field ω_y resulting from the gust encounter with the elastically mounted airfoil is compared for two cases in Fig. 12. The first is the LCO case ($L_g^{x_1}/c = 2$, $A_g/u_\infty = 2$) and the second is the flutter scenario ($L_g^{x_1}/c = 4$, $A_g/u_\infty = 3$). The snapshots of both cases are taken in such a way that the gust center is located at the same x-coordinate. In the first instant (i.e., snapshot I) the gust center is $0.2\,c$ in front of the leading edge. While the LEV is in its initial development stage for the shorter gust, both the LEV and the trailing-edge vortex (TEV) are formed and shed in the longer gust case. This is expected as the gust fully covers the airfoil in the latter case causing an increase in the effective angle of attack throughout the chord length.

In snapshots II and III, the gust center travels and reaches the mid-chord. During this time interval, the TEV resulting from the short gust is generated and shed far from the airfoil in the streamwise direction, whereas the vortices of the long gust are enlarged and vertically convected above the airfoil. The structures formed are similar to those found behind an airfoil immersed in a flow at different angles of attack. At this instant in time, the evaluated average effective angles of attack along the chord length are 58.5° and 70.6° for the short and the long gust, respectively.

In snapshot IV, the gust center arrives at the trailing edge pushing the trailing-edge vortices further from the airfoil. Moreover, it is visible that the gust reverses its influence on the pitch angle as a pitch angle of 0° is restored.

As the gust center starts leaving the TE in snapshot V (gust $0.6\,c$ behind TE), a second TEV is formed in the $L_g^{x_1}/c = 2$ case. Due to the high counterclockwise moment generated by the long gust, a stronger downward pitching motion is observed leading to the shedding of a second LEV.

In snapshot VI, the airfoil–gust encounter is about to end in the $L_g^{x_1}/c = 2$ case and the second TEV is seen to travel in the upstream direction and below the LEV. In the $L_g^{x_1}/c = 4$ case, the second LEV collides with the TEV forming an area of highly disturbed flow. Moreover, due to the longer interaction time lasting 5 dimensionless time units, a second TEV starts to form.

Finally, in snapshots VII and VIII the vortices start to convect downstream in both cases. However, one could notice that for the short gust case nearly no vortices are present within the gust region discernible in Fig. 12 based on the sketch of the gust profile at the bottom of each figure. Instead, main vortices exist either behind or in front of the gust. In contrast, the dispersed vortices of the long gust case coexist with the gust and are convected slightly upwards. This is of great significance when the feedback effect of the structure on the gust is discussed.

Turning the attention to the post-interaction phase, Fig. 13 depicts three snapshots of the total vertical velocity field for both cases when the gust has already left the airfoil. In each instant, the trailing edge of both gusts is at the same distance x_{EE} away from the trailing edge of the airfoil. It can be clearly observed how the shape of the gust velocity profile is radically distorted due to the airfoil–gust interaction. The jet has no longer a continuous 1-cosine shape especially in the shielded area above the airfoil, i.e., $z > 0$. Instead the jet is cut into two halves (see instant I of Fig. 13). While the upper half of the jet freely convects in vertical direction and leaves the computational domain, the lower half of the jet faces the strongly disturbed field in the wake of the airfoil. The flow problem becomes similar to the situation when injecting a transverse jet into a cross-flow but with an injection plane which is continuously moving in streamwise direction. Since the prescribed gust is infinite (equivalent to having a jet supplying nozzle) the lower jet continues to pave its path back in the region above the airfoil (visible in instants II and III of Fig. 13). However, this vertical convection is accompanied by a disturbance-induced jet curvature further downstream. This signifies the capability of the SVM in capturing the full physics of the interaction involved.

5.5. Energy analysis

In order to analyze the motion that the airfoil undergoes due to its interaction with the vertical gust, an energy analysis is conducted. The energies involved are differentiated into the extracted and damped energies. The energy differential extracted by the airfoil from the flow for a degree of freedom z and its corresponding driving force F_z can be written as:

$$dE_{extr} = F_z\,dz = F_z\,\dot{z}\,dt. \tag{21}$$

For an oscillatory motion, the energy extracted per period (T) can be written as:

$$E_{extr} = \int_t^{t+T} F_z\,\dot{z}\,dt. \tag{22}$$

The product ($F_z\,\dot{z}$) shall be referred to as the integrand. The extracted energy for heave and pitch degrees of freedom then reads:

$$E_{h,extr} = \int_t^{t+T} F_L\,\dot{z}\,dt, \tag{23}$$

$$E_{p,extr} = \int_t^{t+T} M_p\,\dot{\alpha}\,dt, \tag{24}$$

where $F_L = F_{\mathrm{CFD},3}$ is the lift force, $\dot{z}$ is the heave velocity, $M_p = M_{\mathrm{CFD},2}$ is the pitching moment, and $\dot{\alpha}$ is the pitch velocity. It is obvious from Eqs. (23) and (24) that the phase shift between the velocity of the degree of freedom and its

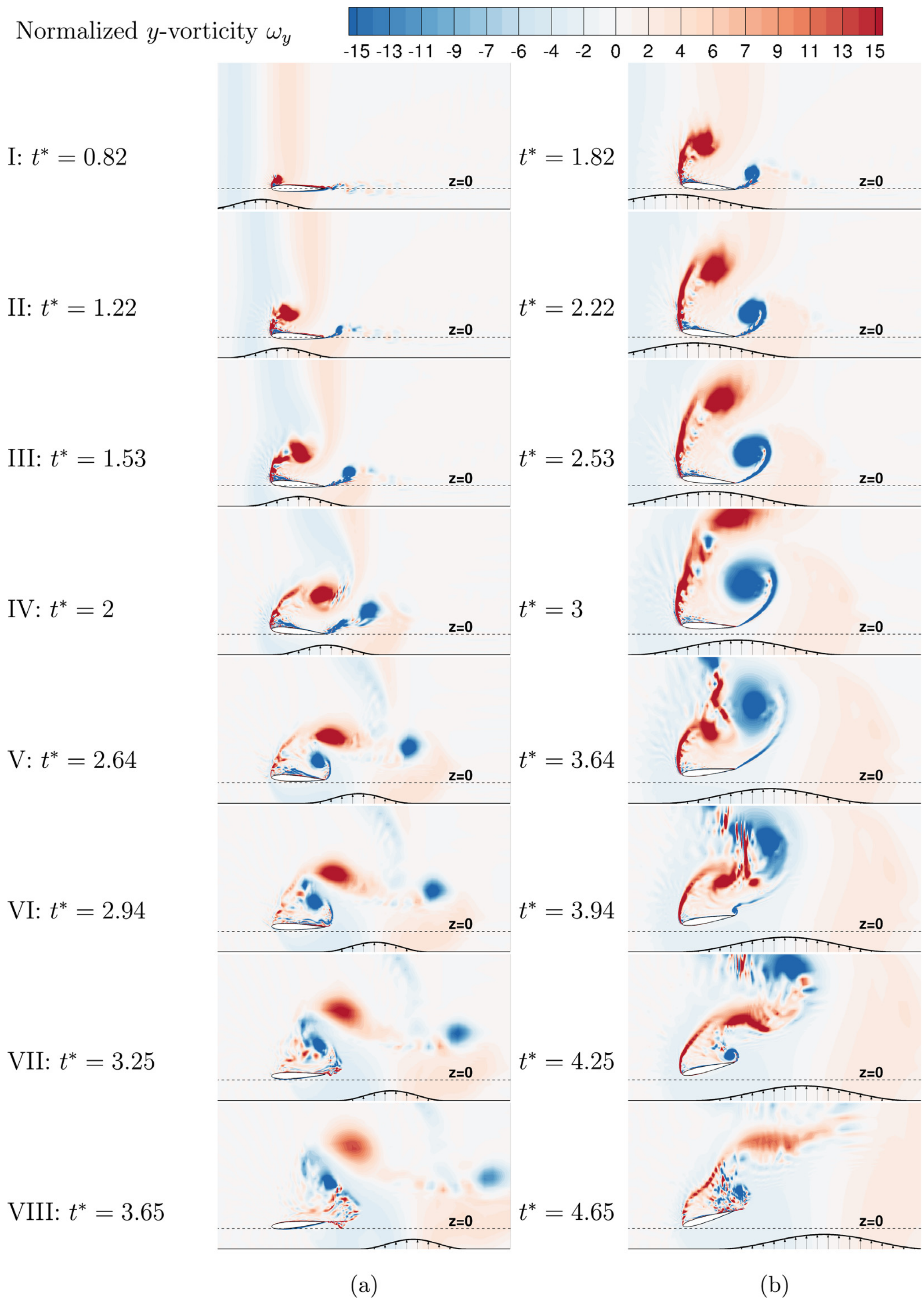

Fig. 12. Eight snapshots of the y-vorticity ω_y of the elastically mounted airfoil. (a) Short gust: $L_g^{x_1}/c = 2$, $A_g/u_\infty = 2$; (b) Long gust: $L_g^{x_1}/c = 4$, $A_g/u_\infty = 3$.

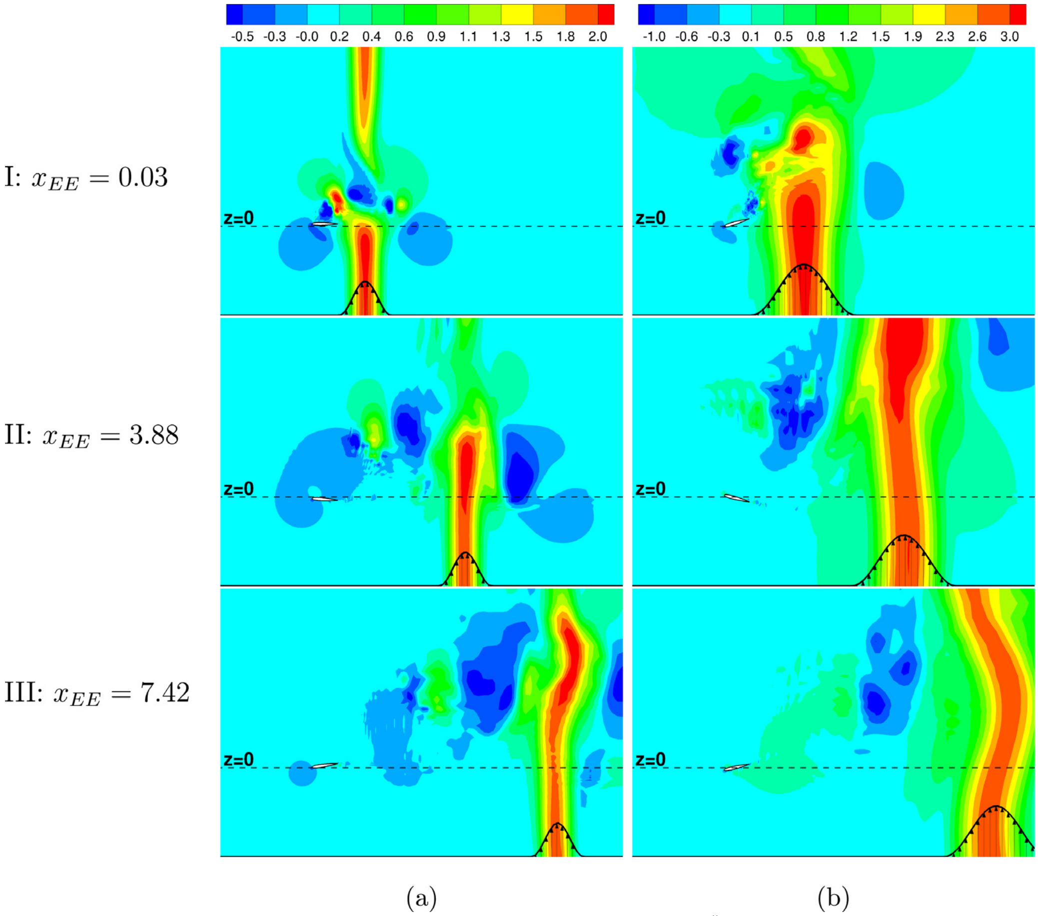

Fig. 13. Post-gust interaction. Total vertical velocity at three time instants. (a) Short gust: $L_g^{x_1}/c = 2$, $A_g/u_\infty = 2$; (b) Long gust: $L_g^{x_1}/c = 4$, $A_g/u_\infty = 3$.

driving force determines whether the flow is feeding the system with energy (i.e., positive E_{extr}) or damping its energy (i.e., negative E_{extr}) (Menon and Mittal, 2019). Similarly, the structural damping energy of each degree of freedom during a single oscillation could be computed by evaluating the integral:

$$E_{h,damp} = \int_t^{t+T} b_h \, \dot{z}^2 \, dt, \tag{25}$$

$$E_{p,damp} = \int_t^{t+T} b_\alpha \, \dot{\alpha}^2 \, dt, \tag{26}$$

where b_h and b_α are the material damping coefficients defined in Section 4. The difference between the extracted and damped energy of a specific degree of freedom defines its total energy:

$$E_{h,total} = E_{h,extr} - E_{h,damp}, \tag{27}$$

$$E_{p,total} = E_{p,extr} - E_{p,damp}. \tag{28}$$

Finally, since energy is a scalar quantity, the total energy of the system is defined by the summation of the total energy of both degrees of freedom:

$$E_{sys,total} = E_{h,total} + E_{p,total}. \tag{29}$$

Note that in the following the energy is made dimensionless with $\frac{1}{2}\rho \, u_\infty^2 A \, c$, where A is the projected area given by $A = l_c \, c$. Figs. 14(a) and 14(c) show the dimensionless DOF, the dimensionless velocity of the corresponding DOF, the driving force coefficient and the dimensionless integrand during one period of the limit-cycle oscillation (here for $L_g^{x_1}/c = 2$ and $A_g/u_\infty = 2$) discussed in Section 5.1. It is worth mentioning that both lift and pitching moment coefficients are low-pass filtered with a cut-off frequency of $f_c = 25$ Hz. Filtering is carried out to facilitate the visualization of the relevant low-frequency dynamics (as this suppresses the short-term fluctuations visible in Fig. 4 and highlights the long-term trend) and to enable a low-frequency range analysis where dominant frequencies exist. Performing such a filtering

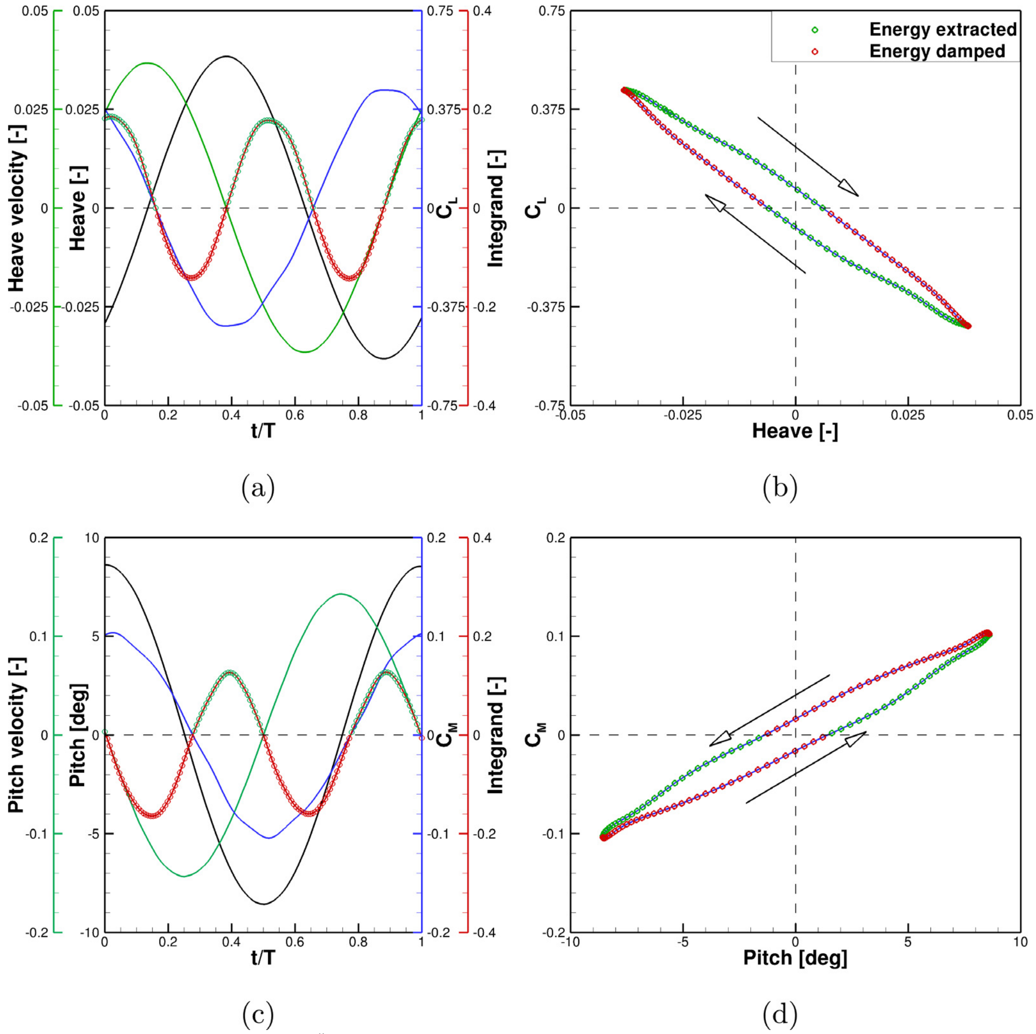

Fig. 14. Analysis within a single LCO cycle for $L_g^{x_1}/c = 2$ and $A_g/u_\infty = 2$. Dimensionless DOF, velocity of the corresponding DOF, aerodynamic coefficient and integrand (a,c), aerodynamic coefficient vs. its respective DOF (b,d). (For interpretation of the references to colour in this figure legend, the reader is referred to the web version of this article.)

was found to be of no influence on the work done by the aerodynamic force and moment as it is insensitive to the high-frequency content contained within these quantities (Poirel et al., 2011). As mentioned earlier, the integrand is a derived quantity obtained by the product of the respective velocity of the DOF by its driving force (i.e., the green curve times the blue curve). The integral of this product (or the area confined between the curve and the x-axis) represents the total dimensionless energy extracted within that period. While the value of this integral is found to be positive for the heave DOF, the interaction of the pitch motion with the flow yields a negative value. This indicates that the flow feeds the airfoil with energy through the heave DOF (i.e., acting as an energy source) and absorbs this energy back from the pitch DOF (i.e., acting as an energy sink). The sum of the interchanged energy between the flow and the airfoil in combination with the total structural damping energies leads to a vanishing total energy as will be shown later.

Figs. 14(b) and 14(d) portray the aerodynamic hysteresis curves by plotting the lift coefficient as a function of the heave and the pitching moment coefficient as a function of the pitch angle during one cycle, respectively. The arrows indicate the direction of advancing time. The green and red circles correspond to those plotted in the integrand curves in Figs. 14(a) and 14(c). They are used to identify the phases in which energy is being extracted from the flow or delivered to the flow. The direction in which the ellipse is formed (clockwise or counterclockwise) indicates the sign of the work done by the aerodynamic coefficients (Poirel et al., 2008). The clockwise rotation in Fig. 14(b) signifies that positive work (or a negative aerodynamic damping) is being imposed by the lift coefficient on the airfoil. In contrast, the counterclockwise rotation seen in Fig. 14(d) points to the overall damping effect that the pitching moment coefficient poses on the airfoil. Thus, the directions of energy transfers for heave and pitch are consistent with the analysis above. Both aerodynamic coefficients mainly show a linear dependency on their respective degrees of freedom. This is unfolded in Figs. 14(a) and 14(c) where the aerodynamic coefficients and the degrees of freedom are sinusoidal functions separated by a phase shift.

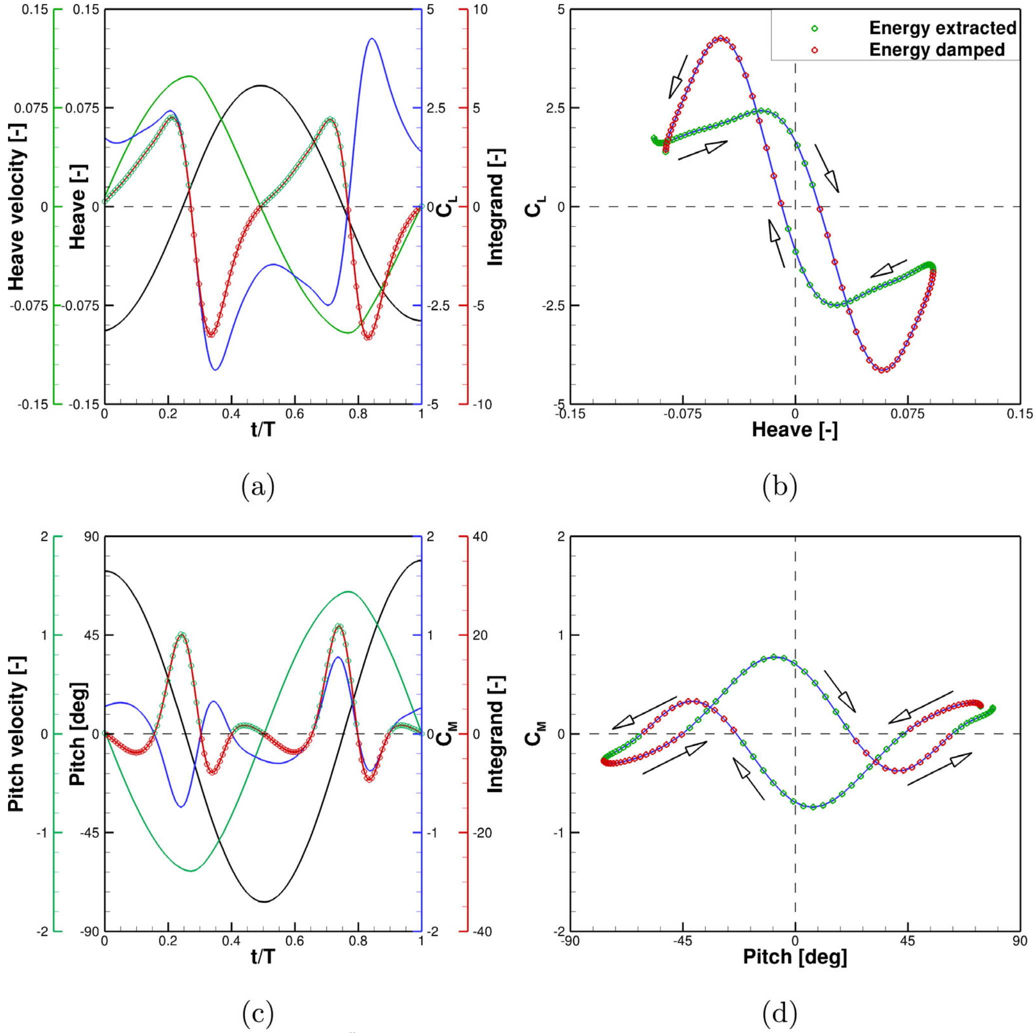

Fig. 15. Analysis within a single diverging cycle for $L_g^{x_1}/c = 4$ and $A_g/u_\infty = 3$. Dimensionless DOF, velocity of the corresponding DOF, aerodynamic coefficient and integrand (a,c), aerodynamic coefficient vs. its respective DOF (b,d).

The linear relationship is even more obvious in Figs. 14(b) and 14(d) where the slope of the formed ring is mainly constant. Note that the product of the slope with $\frac{1}{2}\rho\, u_\infty^2 A$ for the heave and $\frac{1}{2}\rho\, u_\infty^2 A\, c$ for the pitch is interpreted as an equivalent aerodynamic stiffness coefficient by Poirel et al. (2008).

Fig. 15 demonstrates identical relations as those presented in Fig. 14 but for a diverging oscillation (here for $L_g^{x_1}/c = 4$ and $A_g/u_\infty = 3$) leading to flutter. In contrast to the LCO case, the areas evaluated under the heave and pitch integrands are found to be negative and positive, respectively. This indicates that the DOFs have exchanged the roles of energy supply and energy dissipation. Focusing on Figs. 15(a) and 15(c) one could directly distinguish the high non-linearity (non-sinusoidal curves) of the aerodynamic coefficients and the complex distribution of the extracted energy integrands when displayed as a function of their respective DOFs. This is even more evident in Figs. 15(b) and 15(d) where the aforementioned equivalent aerodynamic stiffness coefficients experience sudden changes in their sign and magnitude within one cycle. The source of this non-linear response is attributed to the dynamic stall that the airfoil is undergoing. Indeed, the imposed strong gust excites the pitch DOF of the airfoil to levels exceeding its critical angle of attack (also known as stall angle). It is also worth mentioning that, unlike the LCO case, the loops formed by plotting the aerodynamic coefficients as a function of their respective DOFs switch their direction of turning during the cycle. This indicates that the flow is alternately amplifying (clockwise middle loop) and damping (counterclockwise end loops) the energy of the system within a single cycle.

The energy analysis is now further extended to cover the entire evolution of the different energy components defined in Eqs. (27) to (29) for each DOF. Figs. 16(a) and 16(c) depict the energy components of the heave and pitch DOFs evaluated for their respective cycles of a LCO ($L_g^{x_1}/c = 2$, $A_g/u_\infty = 2$) and a diverging motion ($L_g^{x_1}/c = 4$, $A_g/u_\infty = 3$), respectively. A single period of an oscillation is defined as the time required for a DOF to record two consecutive peaks. Since the DOFs are not in phase, energy components of different DOFs were computed separately. It is also worth mentioning that

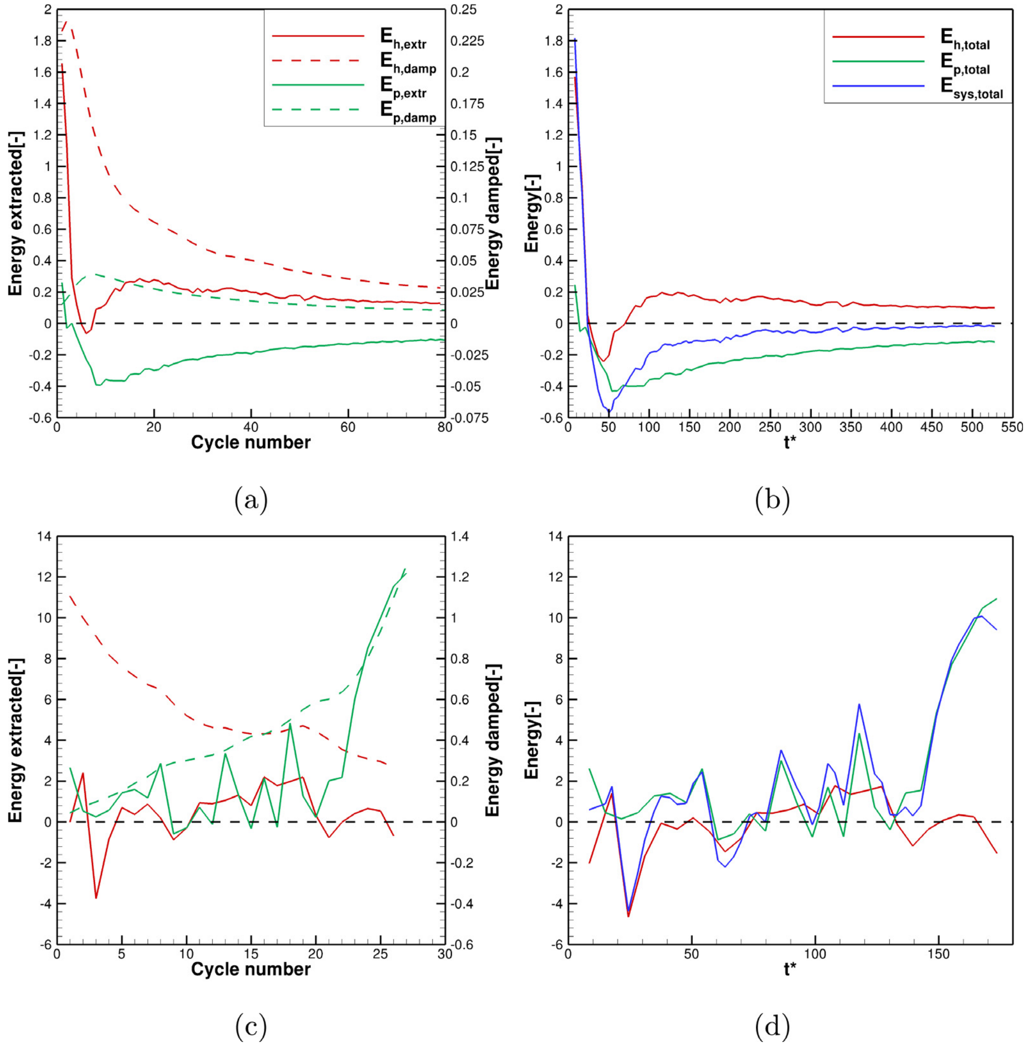

Fig. 16. Analysis of the dimensionless energy for a limit-cycle oscillation case ($L_g^{x_1}/c = 2$ and $A_g/u_\infty = 2$) and a diverging motion case ($L_g^{x_1}/c = 4$ and $A_g/u_\infty = 3$). Heave and pitch extracted and damped energies computed for each respective cycle (a,c), the dimensionless time histories of the instantaneous total energies of both DOFs and the total energy of the system (b,d).

the initial airfoil–gust interaction phase is excluded from the analysis. This phase is eliminated since it contains high energy peaks from which the system's energy starts decaying and rather complex aerodynamic coefficients not following a simple harmonic motion (see zoom-in in Figs. 9 to 11) are observed. Eqs. (27) to (29) are then employed to plot the total heave, pitch and system's energy as a function of the dimensionless time in Figs. 16(b) and 16(d). Focusing on the LCO case, it can be clearly seen in Fig. 16(a) that both DOFs possess an initially positive extracted energy which undergoes a steep decay. This is foreseeable as the flow (including the gust) initially excites and feeds the system with energy in favor of the definition of positive degrees of freedom. The subsequent sharp decrease in the extracted energy is attributed to the airfoil's high kinetic and potential energies being transferred back to the flow in an attempt to achieve a global energy equilibrium. While the extracted energy of the pitch DOF declines below zero and remains negative throughout the simulation time, its heave DOF counterpart stabilizes at positive values. This in turn is in agreement with the finding discussed in Figs. 14(b) and 14(d). The structural damping energies of the heave and pitch DOFs, despite their different magnitudes, show the same behavior. Both energies experience an initial increase attributed to the temporary increase in the velocity of the DOFs followed by a steady decrease to a constant value. The total energies shown in Fig. 16(b) further prove that the system undergoes a LCO motion as the heave and pitch DOFs energies converge to identical values of opposite signs leading to a vanishing total energy of the system.

A completely different outcome is obtained when the same analysis is applied to the diverging motion case. Energy extraction of both DOFs is initially found to be chaotic and not following any perceivable direction (see Fig. 16(c)). The system is seen to gain energy from the flow in some cycles and loosing it in others. This is attributed to the highly transient dynamics (the complex aerodynamic coefficients and the varying phase angle between these coefficients and the velocities of the DOFs) involved in this case caused by the strong gust-induced instability. This behavior is seen until the extracted energy by the pitch DOF starts accumulating. On the other hand, the structural damping energies dictated by the velocities show a clearly recognizable trend. The structural damping of the heave DOF experiences a continuous decrease indicating that its velocity is reducing across the cycles. In contrast, the structural damping of the pitch DOF (and hence its velocity) witnesses a sustained increase until the simulation diverges. The total energies depicted in Fig. 16(d) clearly show that in the case of the diverging motion the main part of the energy is extracted by the pitch motion. That is in clear contrast to the LCO case, where the heave motion was found to be responsible for the energy extraction.

6. Conclusions

The split velocity method combined with a partitioned FSI solver is applied to study the gust-induced oscillations of an elastically mounted NACA 0012 airfoil. This high-fidelity simulation concept relies on an eddy-resolving approach (LES) to guarantee that the most important flow structures are captured, body-fitted block-structured grids (ALE) to resolve the boundary layers and an advanced grid adaptation algorithm (IDW-TFI) to ensure that the high grid quality required for LES is conserved. Choosing a transitional Reynolds number and high gust ratios relevant for MAVs, and a 2-DOF setup with both heave and pitch motion, the following conclusions can be drawn:

- A vertical gust hitting either a fixed ($\alpha = 0°$) or an elastically mounted airfoil from the bottom leads to a strong clockwise rotating leading-edge vortex. That induces a positive peak in the lift and in the pitching moment. During the airfoil–gust interaction (i.e., $t^* \leq 3$ for a gust length $L_g^{x_1}/c = 2$) both the flow fields as well as the forces and moments are nearly identical for the fixed and the elastically mounted airfoil. After the gust has left the airfoil, a limit-cycle oscillation is observed for the heave and pitch motion, whereas in the fixed case the quasi steady-state values are recovered.
- An analysis of the effect of different gust strengths A_g confirms the expectation that the initial heave excitation strongly depends on A_g. Astonishingly that is not the same for the pitch motion.
- For the same gust strength, wider gusts lead to higher amplitudes of the aerodynamic forces and the heave and pitch motion during the airfoil–gust interaction.
- Seven out of nine investigated cases finally end up in limit-cycle oscillations of the airfoil. Although the initial excitation during the gust impact depends on the gust strength and gust length, the amplitudes of the heave and pitch oscillations, which are observed after a long transition period, are all identical for these LCO cases. Thus, the final outcome of these gust impacts is independent of the gust and purely influenced by the non-gust flow interaction with the airfoil dynamics.
- Two out of the nine cases finally induce flutter with a diverging pitch motion. These are the setups with the strongest gusts given by $A_g/u_\infty = 3$ and $L_g^{x_1}/c \geq 4$. The longer the gust is, the faster the extreme pitch excitation is reached.
- The above-mentioned limit between both modes is obviously depending on the parameters defining the system, i.e., inertia, stiffness, and damping parameters as well as x_{EG} and Re number. Nevertheless, the results shown are generic in a sense that a configuration is considered which depending on the strength of excitation due to different gusts ends up in either LCO or flutter.
- By means of an energy analysis the significant differences between the LCO and the flutter case are worked out. The former case is driven by the heave motion, whereas the pitch DOF acts as an energy sink. In the flutter scenario the roles of energy supply and energy dissipation are opposite. Now the pitching motion is powering the coupled system, whereas the heave motion dissipates energy.

Declaration of competing interest

The authors declare the following financial interests/personal relationships which may be considered as potential competing interests: Michael Breuer reports financial support was provided by German Research Foundation.

Data availability

Data will be made available on request.

Acknowledgement

The project is financially supported by the *German Research Foundation (Deutsche Forschungsgemeinschaft)* under the contract number BR 1847/17-1.

Appendix. Evaluation of the near-wall resolution

To evaluate the near-wall resolution of the applied grid, additional LES predictions were carried out for the flow around the fixed airfoil at various angles of attack in the range $0 \leq \alpha \leq 80°$. For this purpose, the inner part of the grid was rotated using the hybrid grid adaption algorithm IDW-TFI described in Section 3.1. Of course, Re and all other parameters of the setup were unchanged. The instantaneous simulations were carried out over a time interval of about twenty vortex shedding cycles. The results were averaged in time and additionally in the homogeneous spanwise direction. Based on the predicted local wall shear stress τ_w, the shear stress velocity u_τ is determined, finally leading to the $y^+ = \Delta y\, u_\tau/\nu$ values of the wall-nearest grid points shown in Fig. A.17. Except for the case of $\alpha = 0°$ the outcome is different for the suction and the pressure side of the airfoil. In the separated flow regions the wall shear stresses are lower leading to y^+

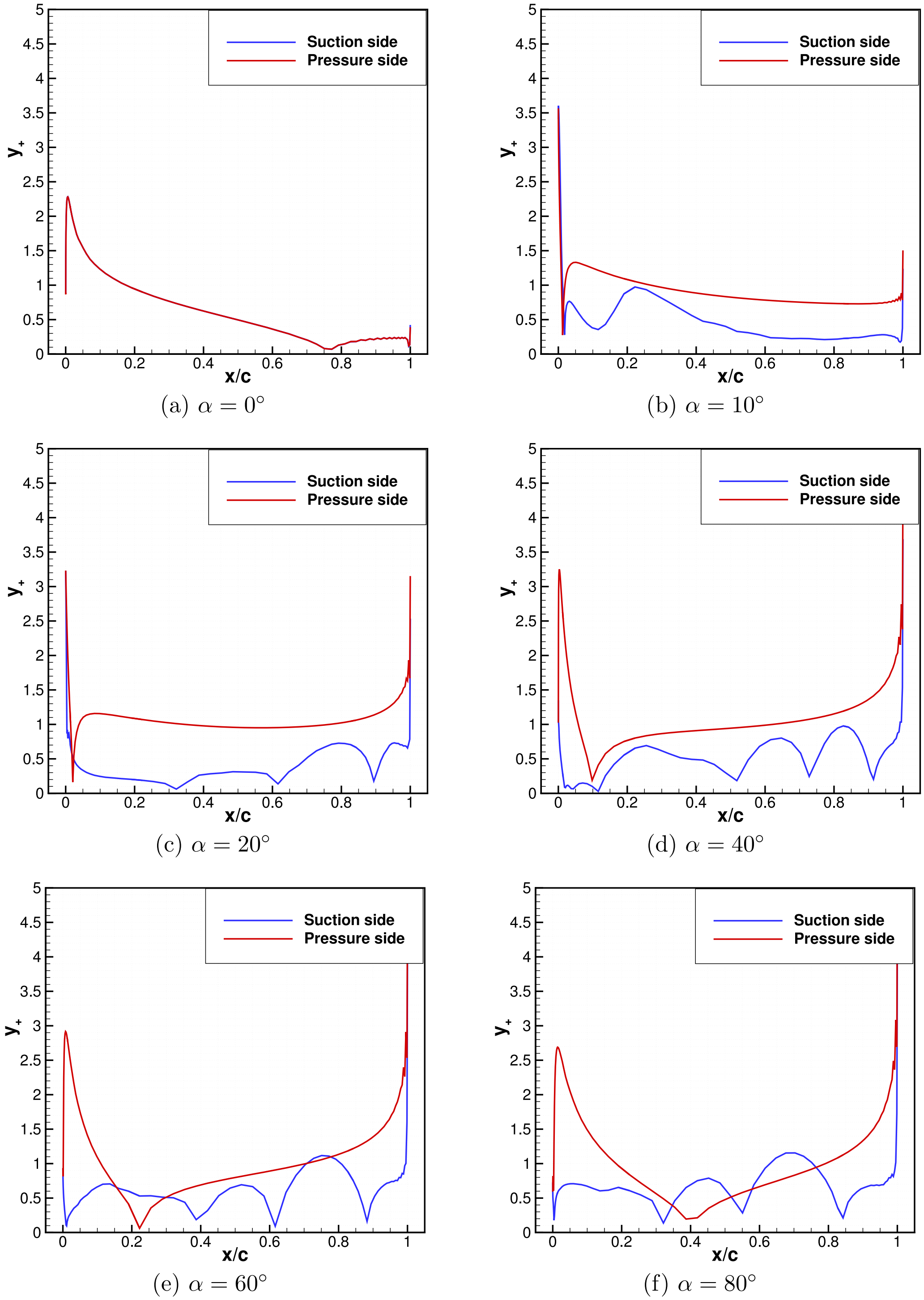

Fig. A.17. Distribution of y^+ of the wall-nearest grid points on the airfoil for six different angles of attack.

values below unity in most regions with the exception of the trailing edge. On the pressure side the values are in general slightly higher but even the peak values are below $y^+ = 5$. Thus, it can be concluded that the dimensionless wall distance is in the range which allows to resolve the viscous sublayer even for the cases with high angles of attack.

References

Andreu-Angulo, I., Babinsky, H., Biler, H., Sedky, G., Jones, A.R., 2020. Effect of transverse gust velocity profiles. AIAA J. 58 (12), 5123–5133.

Apostolatos, A., De Nayer, G., Bletzinger, K.-U., Breuer, M., Wüchner, R., 2019. Systematic evaluation of the interface description for fluid–structure interaction simulations using the isogeometric mortar-based mapping. J. Fluids Struct. 86, 368–399.

Badrya, C., Baeder, J., Jones, A., 2019. Application of prescribed velocity methods to a large-amplitude flat-plate gust encounter. AIAA J. 57 (8), 1–13.

Barnes, C., Visbal, M., 2018a. Gust response of rigid and elastically mounted airfoils at a transitional Reynolds number. Aerosp. Sci. Technol. 74, 112–119.

Barnes, C., Visbal, M., 2018b. On the role of flow transition in laminar separation flutter. J. Fluids Struct. 77, 213–230.

Boulbrachene, K., De Nayer, G., Breuer, M., 2021. Assessment of two wind gust injection methods: Field velocity vs. split velocity method. J. Wind Eng. Ind. Aerodyn. 218, 104790.

Breuer, M., 2018. Effect of inflow turbulence on an airfoil flow with laminar separation bubble: An LES study. Flow Turbul. Combust. 101 (2), 433–456.

Breuer, M., De Nayer, G., Münsch, M., Gallinger, T., Wüchner, R., 2012. Fluid-structure interaction using a partitioned semi-implicit predictor-corrector coupling scheme for the application of large-eddy simulation. J. Fluids Struct. 29, 107–130.

De Nayer, G., Apostolatos, A., Wood, J.N., Bletzinger, K.-U., Wüchner, R., Breuer, M., 2018a. Numerical studies on the instantaneous fluid–structure interaction of an air–inflated flexible membrane in turbulent flow. J. Fluids Struct. 82, 577–609.

De Nayer, G., Breuer, M., 2014. Numerical FSI investigation based on LES: Flow past a cylinder with a flexible splitter plate involving large deformations (FSI-PfS-2a). Int. J. Heat Fluid Flow 50, 300–315.

De Nayer, G., Breuer, M., 2020. A source-term formulation for injecting wind gusts in CFD simulations. J. Wind Eng. Ind. Aerodyn. 207, 104405.

De Nayer, G., Breuer, M., Perali, P., Grollmann, K., 2019. Modeling of wind gusts for large-eddy simulations related to fluid-structure interactions. In: Salvetti, M., Armenio, V., Fröhlich, J., Geurts, B.J., Kuerten, H. (Eds.), ERCOFTAC Series, Direct and Large-Eddy Simulation XI, 11th Int. ERCOFTAC Workshop on Direct and Large-Eddy Simulation: DLES-11, May 29–31, 2017, Vol. 25. Springer Nature Switzerland AG 2019, pp. 453–459.

De Nayer, G., Breuer, M., Wood, J.N., 2020. Numerical investigations on the dynamic behavior of a 2-DOF airfoil in the transitional Re number regime based on fully coupled simulations relying on an eddy-resolving technique. Int. J. Heat Fluid Flow 85, 108631.

De Nayer, G., Kalmbach, A., Breuer, M., Sicklinger, S., Wüchner, R., 2014. Flow past a cylinder with a flexible splitter plate: A complementary experimental-numerical investigation and a new FSI test case (FSI-PfS-1a). Comput. & Fluids 99, 18–43.

De Nayer, G., Schmidt, S., Wood, J.N., Breuer, M., 2018b. Enhanced injection method for synthetically generated turbulence within the flow domain of eddy-resolving simulations. Comput. Math. Appl. 75 (7), 2338–2355.

Demirdžić, I., Perić, M., 1988. Space conservation law in finite-volume calculations of fluid flow. Int. J. Numer. Methods Fluids 8 (9), 1037–1050.

Demirdžić, I., Perić, M., 1990. Finite-volume method for prediction of fluid flow in arbitrarily shaped domains with moving boundaries. Int. J. Numer. Methods Fluids 10 (7), 771–790.

Dowell, E., Edwards, J., Strganac, T., 2003. Nonlinear aeroelasticity. J. Aircr. 40 (5), 857–874.

Dowell, E.H., Tang, D., 2002. Nonlinear aeroelasticity and unsteady aerodynamics. AIAA J. 40 (9), 1697–1707.

Durst, F., Schäfer, M., 1996. A parallel block-structured multigrid method for the prediction of incompressible flows. Int. J. Numer. Methods Fluids 22 (6), 549–565.

Ekaterinaris, J.A., Platzer, M.F., 1998. Computational prediction of airfoil dynamic stall. Prog. Aerosp. Sci. 33 (11), 759–846.

Eldredge, J.D., Jones, A.R., 2019. Leading-edge vortices: Mechanics and modeling. Annu. Rev. Fluid Mech. 51 (1), 75–104.

Galbraith, M.C., Visbal, M.R., 2009. Implicit large–eddy simulation of low–Reynolds number transitional flow past the SD7003 airfoil. In: 46th AIAA Aerospace Sciences Meeting and Exhibit, 7–10 January 2008, Reno, Nevada. URL https://doi.org/10.2514/6.2008-225.

Heinrich, R., Reimer, L., 2013. Comparison of different approaches for gust modeling in the CFD code TAU. In: International Forum on Aeroelasticity & Structural Dynamics 2013. URL https://elib.dlr.de/85834/.

Huntley, S.J., Jones, D., Gaitonde, A., 2016. 2D and 3D gust response using a prescribed velocity method in viscous flows. In: 46th AIAA Fluid Dynamics Conference. American Institute of Aeronautics and Astronautics, pp. 1–15.

Huntley, S.J., Jones, D., Gaitonde, A., 2017. Aeroelastic gust response of an aircraft using a prescribed velocity method in viscous flows. In: 23rd AIAA Computational Fluid Dynamics Conference. American Institute of Aeronautics and Astronautics, Denver, Colorado, pp. 1–18.

IEC-Standard, 2002. 61400-21. Tech. rep..

Kalmbach, A., Breuer, M., 2013. Experimental PIV/V3V measurements of vortex–induced fluid–structure interaction in turbulent flow — A new benchmark FSI–PfS–2a. J. Fluids Struct. 42, 369–387.

Leroyer, A., Visonneau, M., 2005. Numerical methods for RANSE simulations of a self-propelled fish-like body. J. Fluids Struct. 20 (7), 975–991.

Lesoinne, M., Farhat, C., 1996. Geometric conservation laws for flow problems with moving boundaries and deformable meshes, and their impact on aeroelastic computations. Comput. Methods Appl. Mech. Engrg. 134 (1–2), 71–90.

Lobo, B.A., Özçakmak, Ö.S., Madsen, H.A., Schaffarczyk, A.P., Breuer, M., Sørensen, N.N., 2022. On the laminar-turbulent transition mechanism on Megawatt wind turbine blades operating in atmospheric flow. Wind Energy Sci. URL https://doi.org/10.5194/wes-2022-42.

McCroskey, W.J., 1982. Unsteady airfoils. Annu. Rev. Fluid Mech. 14 (1), 285–311.

Mellen, C.P., Fröhlich, J., Rodi, W., 2003. Lessons from LESFOIL project on large-eddy simulation of flow around an airfoil. AIAA J. 41 (4), 573—581.

Menon, K., Mittal, R., 2019. Flow physics and dynamics of flow-induced pitch oscillations of an airfoil. J. Fluid Mech. 877, 582–613.

Menon, K., Mittal, R., 2020. Aeroelastic response of an airfoil to gusts: Prediction and control strategies from computed energy maps. J. Fluids Struct. 97, 103078.

Newmark, N.M., 1959. A method of computation for structural dynamics. J. Eng. Mech. Div. 85 (3), 67–94.

Perrotta, G., Jones, A.R., 2017. Unsteady forcing on a flat-plate wing in large transverse gusts. Exp. Fluids 58 (101).

Poirel, D., Harris, Y., Benaissa, A., 2008. Self-sustained aeroelastic oscillations of a NACA 0012 airfoil at low-to-moderate Reynolds numbers. J. Fluids Struct. 24, 700–719.

Poirel, D., Métivier, V., Dumas, G., 2011. Computational aeroelastic simulations of self-sustained pitch oscillations of a NACA 0012 at transitional Reynolds numbers. J. Fluids Struct. 27, 1262–1277.

Poirel, D., Yuan, W., 2010. Aerodynamics of laminar separation flutter at a transitional Reynolds number. J. Fluids Struct. 26, 1174–1194.

Poudel, N., Yu, M., Hrynuk, J.T., 2021. Gust mitigation with an oscillating airfoil at low Reynolds number. Phys. Fluids 33 (10), 101905.

Schmidt, S., 2016. Entwicklung einer hybriden LES–URANS Methode für interne und externe Strömungen (Ph.D. thesis). Professur für Strömungsmechanik, Helmut–Schmidt–Universität, Hamburg, Germany, URL https://openhsu.ub.hsu-hh.de/handle/10.24405/4295.

Schmidt, S., Breuer, M., 2014. Hybrid LES–URANS methodology for the prediction of non–equilibrium wall–bounded internal and external flows. Comput. & Fluids 96, 226–252.
Schmidt, S., Breuer, M., 2017. Source term based synthetic turbulence inflow generator for eddy–resolving predictions of an airfoil flow including a laminar separation bubble. Comput. & Fluids 146, 1–22.
Sen, S., De Nayer, G., Breuer, M., 2017. A fast and robust hybrid method for block-structured mesh deformation with emphasis on FSI-LES applications. Int. J. Numer. Methods Eng. 111 (3), 273–300.
Smagorinsky, J., 1963. General circulation experiments with the primitive equations I: The basic experiment. Mon. Weather Rev. 91 (3), 99–165.
Theodorsen, T., 1935. General Theory of Aerodynamic Instability and the Mechanism of Flutter. NACA Report 496.
Visbal, M.R., Gordnier, R.E., Galbraith, M.C., 2009. High–fidelity simulations of moving and flexible airfoils at low Reynolds numbers. Exp. Fluids 46, 903–922.
von Kármán, T., Sears, W.R., 1938. Airfoil theory for non-uniform motion. J. Aeronaut. Sci. 5 (10), 379–390.
Wales, C., Jones, D., Gaitonde, A., 2014. Prescribed velocity method for simulation of aerofoil gust responses. J. Aircr. 52 (1), 64–76.
Wood, J.N., Breuer, M., De Nayer, G., 2018. Experimental studies on the instantaneous fluid–structure interaction of an air–inflated flexible membrane in turbulent flow. J. Fluids Struct. 80, 405–440.
Wood, J.N., Breuer, M., De Nayer, G., 2020. Experimental investigations on the dynamic behavior of a 2-DOF airfoil in the transitional Re number regime based on digital-image correlation measurements. J. Fluids Struct. 96, 103052.
Wood, J.N., De Nayer, G., Schmidt, S., Breuer, M., 2016. Experimental investigation and large-eddy simulation of the turbulent flow past a smooth and rigid hemisphere. Flow Turbul. Combust. 97 (1), 79–119.
Yuan, W., Poirel, D., Wang, B., 2013. Simulations of pitch-heave limit-cycle oscillations at a transitional Reynolds number. AIAA J. 51 (7), 1716–1732.